THE ROLE OF PLACE CELLS AND GRID CELLS IN SPATIAL NAVIGATION

Doctoral Dissertation, 2012

ZSÓFIA HUHN

Department of Biophysics KFKI Research Institute for Particle and Nuclear Physics of the Hungarian Academy of Sciences, Budapest, Hungary

Advisors:
Dr. Péter Érdi, Ph.D. D.Sc., Henry R. Luce Professor, Head of Department
Dr. Zoltán Somogyvári, Ph.D.

Faculty of Sciences, Eötvös Loránd University, Budapest, Hungary

Ph.D. School: Biology
Head: Dr. Anna Erdei

Ph.D. Program: Neuroscience and Human Biology
Head: Dr. László Détári

“The facts are friendly... Especially in our early investigations I can well remember the anxiety of waiting to see how the findings came out. Suppose our hypotheses were disproved! Suppose we were mistaken in our views! Suppose our opinions were not justified! At such times, as I look back, it seems to me that I regarded the facts as potential enemies, as possible bearers of disaster. I have perhaps been slow in coming to realize that the facts are always friendly. Every bit of evidence one can acquire, in any area, leads one that much closer to what is true. And being closer to the truth can never be a harmful or dangerous or unsatisfying thing. So while I still hate to readjust my thinking, still hate to give up old ways of perceiving and conceptualizing, yet at some deeper level I have, to a considerable degree, come to realize that these painful reorganizations are what is known as learning, and that though painful they always lead to a more satisfying because somewhat more accurate way of seeing life... I feel sure the facts will be my friends.”

Carl Rogers: *On becoming a person*

Acknowledgements

This work was carried out in the Computational Neuroscience Group, Department of Biophysics at the KFKI Research Institute for Particle and Nuclear Physics of the Hungarian Academy of Sciences between 2004-2006 and 2008-2010. I would like to express my gratitude to the head of the group, Dr. Péter Érdi for supporting me in rejoining his group and continuing my doctoral research in the field of computational neuroscience.

I would also like to thank to my advisor in the place cell research, Dr. Máté Lengyel for introducing me to computational neuroscience and teaching the basic techniques of single cell modeling.

I am very grateful to my second advisor, Dr. Zoltán Somogyvári for always being ready to discuss any little part of the distance model. Thanks to his strict mathematical approach, precise analytic calculations on the cell numbers in distance cell models could be worked out.

I thank Dr. Balázs Ujfalussy for providing me his latex codes that helped a lot in document formatting.

Also, thanks to all other members of the lab for their helpfulness and for the friendly atmosphere of the group.

I am also very grateful to my family for supporting me with all means in working on my doctoral research and dissertation.

Contents

List of Figures

1

Introduction

One of the main animal behaviors is locomotion, movement by which the animal changes the position of its whole body. While observing moving mammals we usually feel that this movement is not a random roaming, it rather seems to be a conscious and planned behavior. They sense and perceive stimuli, recognize landmark cues and places, determine and estimate distances and directions, recall spatial memories about the known environment and make decisions on the future movement actions (turning, moving, stopping etc.). This is what we call *navigation* in everyday life. But what exactly is spatial navigation according to the scientists?

According to Gallistel (1990): "Navigation is the process of determining and maintaining a course or trajectory from one place to another. Processes for estimating one's position with respect to the known world are fundamental to it. The known world is composed of the surfaces whose locations relative to one another are represented on a map. "

This definition contains the hypotheses, that there is a "map in the brain". However, definitions of this *cognitive map* are diverse and often conflicting. It is thus necessary to define in a more concrete way what navigation is and what the functions of a navigation system are. According to Levitt and Lawton (1990), navigation is defined by the following three questions: (a) "Where am I?"; (b) "Where are other places relative to me?"; and (c) "How do I get to other places from here?" Underlying question (a) is the problem of recognizing and identifying the particular place in which the animal is situated. Question (b) amounts to processing a global spatial representation — for instance, a spatial relation network where every other position has a known relation to the current place. These first two questions build up the necessary framework from which the appropriate action can be derived, i.e. the object of question (c). Note that this last question involves a notion of "planning" i.e. asking for the whole trajectory from the current location to the considered goal

location.

According to other authors (Trullier et al., 1997), these definitions of navigation are too restrictive, since navigation is possible without processing a global spatial representation and without planning. In the followings we distinguish and define seven different navigational strategies of increasing complexity:

1. *Random navigation*: when the animal has no information about the environment, it randomly moves and collects information about it.

2. *Taxon navigation*: the animal finds a cue and moves toward it. This is a basic ability in every higher order navigation strategy.

3. *Praxic navigation*: the animal automatically executes a constant motor program that was practiced before. During practicing the animal memorized what physical actions (turning, stopping, etc.) in which order it has to do in order to reach the goal. This strategy works only if the spatial relation between the starting point and the goal is invariable.

4. *Guidance navigation*: at the goal the animal memorizes the spatial relationship between itself and the landmark configuration. When the animal tries to find the goal it continuously compares the actually perceived and the memorized sensory information (or computed attributes like distance or direction from a certain landmark). The movement is appropriate when the discrepancy between the current and the required state of the sensors decreases. This type of navigation can be used only if cues can be perceived at the goal location (i.e. landmarks are not too far from it).

5. *Place recognition-triggered navigation*: the animal first recognizes its location, chooses and follows the appropriate direction until reaching a new known place (stimulus-response type of behavior). It continues to repeat these actions until reaching the goal. The animal always chooses the very next action instead of planning the whole sequence of future movements. It does not store an internal representation on the relations between places, it only memorizes landmark configurations defining places and the appropriate moving directions belonging to these places. As a consequence, if the animal meets an unexpected obstacle, it can not plan an alternative route. It has to wander randomly until reaching another known place from which the goal can be reached through a different route.

6. *Topologic navigation*: similarly to the previous, the animal associates directions to places but it is already able to predict the place which it reaches by following the appropriate direction (stimulus-response-stimulus type of behavior). By this ability the animal is able to plan the whole sequence of movements and memorize the whole trajectory. If it runs into obstacles, it is able to plan an alternative trajectory by combining the already known route parts. Thus, the animal has a representation on the spatial relations of places, the *topology* of the environment. A disadvantage of this strategy is that the animal only travels through already known places: it chooses the known trajectory, even if there would be a previously not visited but shorter route.

7. *Metric navigation*: the animal represents metric information — distances and angles between places, thus it uses an internalized metric map. By this strategy the animal is able to compute and plan the optimal trajectory, find shortcuts to the goal or make the shortest detour when bumping into unpredicted obstacles.

As seen above, any higher order navigation strategy needs the ability of place recognition and representation and the most complex one also needs the storage of directions and distances between places.

In the present dissertation place and distance representations are studied in rodents at the single cell and network levels by means of computational modeling. In the first part *place cells* are studied which are the principal cells of the brain region *hippocampus* in rodents and encode the spatial location of the animal. A place cell fires only when the rat traverses a particular portion of the environment, called the *place field* of the cell. Firing activity of place cells thus show a strong correlation with the spatial position of the animal. Furthermore, they encode the spatial position of the animal both by their firing rate and the precise timing of their firings. *Rate coding* implies that during a single traversal, firing frequency of the cell increases in the early and decreases in the late portion of the place field. *Phase coding* was demonstrated as a monotonic decrease in the phase of firings relative to the ongoing theta oscillation during a single traversal. Place cell activity and the generation of rate and phase code are studied on a biophysical conductance-based cell model containing a dendrite and a soma compartment. Long-term integration of dendritic inputs and intrinsic dendritic dynamics were studied in detail. As we found that dendritic long term integration could lead to persistent neural activity (changed cell activity

lasting several seconds after transient stimulation), analysis of place cell activity is discussed from the broader perspective of long-term integration and persistent activity in single cells.

The second part of this dissertation is about the neural representation of distance among places, which is necessary to perform metric navigation. In 2005, the *grid cells* were discovered in the *medial entorhinal cortex* of rats, which show a new type of position dependent firing activity. These cells were shown to be active when the animal occupies the vertices of a triangular grid tessellating the plane. This grid cell system is considered as an explicit example of metric space representation in the central nervous system. However, due to the periodic nature of this spatial code, extraction of distance information from grid cells is not straightforward. Here we propose a biologically realistic mechanism for this computation and a network model is set up to study the neural mechanism of distance information decoding from the ensemble of grids cells. Analytical calculations are done on the capacity and effectiveness of this system and the precision of distance coding is studied by numerical simulations. Finally, the firing pattern of the model cells to real cell activities is compared and a prediction is given on the location of the hypothesized distance encoding cells.

2

Place representation

2.1 Introduction

Pyramidal cells in the cerebral cortex have extended dendritic arbors integrating inputs from thousands of presynaptic cells (Hausser et al., 2000). Active voltage-dependent conductances play a central role in shaping this integration process: they can boost distal inputs so that their effect on somatic firing becomes level with that of proximal inputs (Cook and Johnston, 1997), make the summation of postsynaptic potentials (PSPs) sub- or supra-linear defying the predictions of standard cable theory (Rall, 1959, 1989), and hence endow single neurons with computational powers identical to those of a network of point-neurons (Poirazi et al., 2003). In some cases, sufficiently strong stimulation is able to elicit dendritic spikes (Kandel and Spencer, 1961; Wong et al., 1979) which thus represent an extreme case of these non-linear processing capabilities. Such dendritic regenerative potentials are considered to be the final outcomes of local dendritic integration which ultimately influence somatic action potential generation (Golding and Spruston, 1998) or local synaptic plasticity (Golding et al., 2002).

Most of the studies of non-linear dendritic processing focused on the spatial aspects of integration, while its temporal aspects have attracted relatively little attention. In this paradigm, PSPs are integrated in a potentially complicated way to produce a change in dendritic membrane potential depending on their amplitudes, slopes, and dendritic locations, but the membrane potential at any time only depends on the immediate past of the neuron's input (Reyes, 2001). Crucially, the window of temporal integration is assumed to be small, as it is determined by the time constants of the PSPs and the membrane time constant, none of which exceeds usually tens of milliseconds (Rall, 1989; Destexhe et al., 1998).

Active conductances seem to further reduce the effective time constant of den-

drites. Although dendritic cable filtering may smear out distally evoked PSPs by the time they reach the soma so that they summate on a longer time scale (Rall, 1959), a voltage-dependent current, the hyperpolarization-activated I_{h} current, was shown to counteract this and produce location-independent PSP time-courses in the soma (Magee, 1999). Plateau potentials (see below) are also actively terminated by voltage- and Ca^{2+}-dependent currents in pyramidal cells (Wei et al., 2001). This seems to be at odds with findings showing that many neuron types including cortical pyramidal cells are able to integrate inputs on long time scales. The most striking example of this is when transient inputs lead to persistent changes in neural firing rates that last for several hundred milliseconds or even seconds (Major and Tank, 2004).

While proposed network mechanisms for generating persistent neural activity proliferate (Seung, 1996; Koulakov et al., 2002; Goldman et al., 2003; Machens et al., 2005), it is less understood what properties of single neurons may favor long time scale integration (Marder et al., 1996). Bistability of the membrane potential through self sustaining plateau potentials is an often advocated single cell mechanism that has been recently confirmed in Purkinje cells *in vivo* (Loewenstein et al., 2005). Plateau potentials have also been demonstrated in pyramidal cells, but they require excessive stimulation and terminate relatively fast after the cessation of the stimulus (Schwindt and Crill, 1999; Wei et al., 2001). Furthermore, because plateau potentials are all-or-none events, intricate mechanisms have to be invoked to explain graded integrative responses (Goldman et al., 2003).

Another often neglected factor is the effect that ongoing *in vivo* population activity has on the way a neuron integrates its inputs. Intense bombardment of the dendritic tree with synaptic inputs is characteristic of *in vivo* states (Destexhe et al., 2003) and was shown to decrease the membrane resistance (Williams, 2004). As a consequence, it should also decrease the membrane time constant (Bernander et al., 1991) thereby further reducing the effective time scale of dendritic integration. In accordance with this, morphologically and electrophysiologically realistic computational modeling showed that neurons can process their inputs with a high temporal resolution under these conditions (Rudolph and Destexhe, 2003a). However, previous studies used constant (Williams, 2004) or stationary (Bernander et al., 1991; Rudolph and Destexhe, 2003a,b) background activity as a model of *in vivo* network activity while cortical networks are known to exhibit behavior-dependent oscillations on several time scales (Buzsáki and Draguhn, 2004). In particular, execution

of working memory tasks, for which persistent activity seems to be crucial, is often accompanied by cortical theta oscillations (Gevins et al., 1997; Tesche and Karhu, 2000; Jensen and Tesche, 2002). Moreover, blocking theta was shown to cause impairment in these tasks (Winson, 1978; Givens and Olton, 1990; Mizumori et al., 1990).

Here we use a simplified biophysical model neuron to investigate how periodic dendritic spiking contributes to the integration of inputs on long time scales during one of the most prominent brain rhythms, the hippocampal theta oscillation (Buzsáki, 2002). *In vivo* population activity was shown to facilitate the compartmentalization of dendrites, so that they integrate their inputs independently of somatic events (Williams, 2004), and also to promote the generation and propagation of dendritic spikes (Destexhe and Pare, 1999; Williams, 2004). Regular dendritic spiking was observed in the hippocampus during theta oscillations (Kamondi et al., 1998; Gillies et al., 2002), and the frequency of dendritic oscillations could be modulated by the amount of injected current (Kamondi et al., 1998). We propose that under these conditions periodic dendritic spiking integrates inputs in its spiking phase relative to the ongoing field potential oscillation, and the decay time constant of this integration can be several orders of magnitude longer than the membrane time constant.

The somatic membrane potential of hippocampal pyramidal is periodically modulated during theta oscillations (Leung and Yim, 1986; Soltész and Deschenes, 1993; Ylinen et al., 1995), and the ability of dendritic spikes evoking somatic action potentials was shown to depend on the level of somatic depolarization (Golding and Spruston, 1998; Williams, 2004). We show that this provides a potential mechanism for transforming the phase code of dendritic spikes into a firing rate code, as the number of somatic action potentials fired within a theta cycle depends on the phase of the dendritic spike relative to the somatic membrane potential oscillation. The phase of somatic action potentials also reflects the phase of the dendritic spike, but it can be decoupled from the rate code by changing levels of somatic depolarization, so that the firing phase and rate of a cell code for different variables, just as seen in recent experiments in behaving animals (Huxter et al., 2003). We test further predictions of our model on the firing patterns of hippocampal pyramidal cells by comparing them to data recorded from place cells in rats.

2.2 Model

We used a modified Pinsky-Rinzel (Pinsky and Rinzel, 1994) two compartmental conductance-based model of a hippocampal CA3 pyramidal cell. Somatic and dendritic membrane potentials obeyed standard current balance equations:
$C_{\mathrm{m}}\dot{V}_{\mathrm{s}}(t) = -I_{\mathrm{Ls}}(t) - I_{\mathrm{Na}}(t) - I_{\mathrm{K-DR}}(t) + I_{\mathrm{As}}(t) + I_{\mathrm{s}}(t)$, and
$C_{\mathrm{m}}\dot{V}_{\mathrm{d}}(t) = -I_{\mathrm{Ld}}(t) - I_{\mathrm{Ca}}(t) - I_{\mathrm{K-C}}(t) + I_{\mathrm{Ad}}(t) + I_{\mathrm{d}}(t)$.
Leak currents were:
$I_{\mathrm{Ls}}(t) = g_{\mathrm{L}}\,[V_{\mathrm{s}}(t) - V_{\mathrm{L}}]$ and
$I_{\mathrm{Ld}}(t) = g_{\mathrm{L}}\,[V_{\mathrm{d}}(t) - V_{\mathrm{L}}]$.
Axial currents were:
$I_{\mathrm{As}}(t) = g_{\mathrm{c}}/p\;[V_{\mathrm{d}}(t) - V_{\mathrm{s}}(t)]$ and
$I_{\mathrm{Ad}}(t) = g_{\mathrm{c}}/(1-p)\;[V_{\mathrm{s}}(t) - V_{\mathrm{d}}(t)]$.
Voltage-dependent currents were:
the fast Na^+ current $I_{\mathrm{Na}}(t) = g_{\mathrm{Na}}\, m_{\infty}^3(t)\, h(t)\;[V_{\mathrm{s}}(t) - V_{\mathrm{Na}}]$,
the delayed rectifier K^+ current $I_{\mathrm{K-DR}}(t) = g_{\mathrm{K-DR}}\, n^4(t)\;[V_{\mathrm{s}}(t) - V_{\mathrm{K}}]$,
the non-inactivating Ca^{2+} current $I_{\mathrm{Ca}}(t) = g_{\mathrm{Ca}}\, s^4(t)\;[V_{\mathrm{d}}(t) - V_{\mathrm{Ca}}]$,
and the Ca^{2+}-dependent K^+ current $I_{\mathrm{K-C}}(t) = g_{\mathrm{K-C}}\, c(t)\;\;\chi(t)\,[V_{\mathrm{d}}(t) - V_{\mathrm{K}}]$,
where $\chi(t) = \min[Ca(t)\,/750, 1]$ and $\dot{Ca}(t) = -0.13\, I_{\mathrm{Ca}}(t) - 0.075\, Ca(t)$.
Gating variables m, h, n, s and c obeyed first order kinetics: for any x gating variable $\dot{x}(t) = \alpha_x[V(t)]\;[1 - x(t)] - \beta_x[V(t)]\;x(t)$, however m was approximated with its steady-state value $m_{\infty}(t) = \alpha_m[V(t)]\;/\;\{\alpha_m[V(t)] + \beta_m[V(t)]\}$.
Rate variables were:
$\alpha_m[V_{\mathrm{s}}(t)] = 0.32\;[-46.9 - V_{\mathrm{s}}(t)]\;/\;(\exp\{[-46.9 - V_{\mathrm{s}}(t)]\,/4\} - 1)$,
$\beta_m[V_{\mathrm{s}}(t)] = 0.28\;[V_{\mathrm{s}}(t) + 19.9]\;/\;(\exp\{[V_{\mathrm{s}}(t) + 19.9]\,/5\} - 1)$,
$\alpha_h[V_{\mathrm{s}}(t)] = 0.128\exp\{[-43 - V_{\mathrm{s}}(t)]\,/18\}$, $\beta_h[V_{\mathrm{s}}(t)] = 4/\,(1 + \exp\{[-20 - V_{\mathrm{s}}(t)]\,/5\})$,
$\alpha_n[V_{\mathrm{s}}(t)] = 0.016\;\;[-24.9 - V_{\mathrm{s}}(t)]\;/\;(\exp\{[-24.9 - V_{\mathrm{s}}(t)]\,/5\} - 1)$,
$\beta_n[V_{\mathrm{s}}(t)] = 0.25\;\exp\{0.5 - 0.025\;[V_{\mathrm{s}}(t) + 60]\}$,
$\alpha_s[V_{\mathrm{d}}(t)] = 1.6/\,(1 + \exp\{-0.072\;[V_{\mathrm{d}}(t) - 5]\})$,
$\beta_s[V_{\mathrm{d}}(t)] = 0.02\;\;[V_{\mathrm{d}}(t) + 8.9]\;/\;(\exp\{[V_{\mathrm{d}}(t) + 8.9]\,/5\} - 1)$,
$\alpha_c[V_{\mathrm{d}}(t)] = \exp\{[V_{\mathrm{d}}(t) + 50]\,/11 - [V_{\mathrm{d}}(t) + 53.5]\,/27\}\,/18.975{\cdot}\mathcal{H}[-V_{\mathrm{d}}(t) - 10] +$
$2\,\exp\{[-V_{\mathrm{d}}(t) - 53.5]\,/27\}\cdot\mathcal{H}[V_{\mathrm{d}}(t) + 10]$,
$\beta_c[V_{\mathrm{d}}(t)] = (2\,\exp\{[-V_{\mathrm{d}}(t) - 53.5]\,/27\} - \alpha_c[V_{\mathrm{d}}(t)])\cdot\mathcal{H}[-V_{\mathrm{d}}(t) - 10]$, where $\mathcal{H}$ is the Heaviside function.

Passive parameters of the model were: $C_{\mathrm{m}} = 1\,\mu\mathrm{F/cm}^2$ membrane capacitance,

$g_{\mathrm{L}} = 0.3\,\mathrm{mS/cm^2}$ leak conductance (except in Figure 2.2Ab), $V_{\mathrm{L}} = -60\,\mu\mathrm{V}$ leak reversal potential, $g_{\mathrm{c}} = 0.005\,\mathrm{mS/cm^2}$ axial conductance between the soma and the dendrite, and $p = 0.1$ soma/cell surface area ratio. Equilibrium potentials (in mV) and maximal channel conductances (in $\mathrm{mS/cm^2}$) of active conductances were $V_{\mathrm{Na}} = 60$, $V_{\mathrm{K}} = -75$, $V_{\mathrm{Ca}} = 80$, and $g_{\mathrm{Na}} = 30$, $g_{\mathrm{K-DR}} = 15$, $g_{\mathrm{Ca}} = 10$, $g_{\mathrm{K-C}} = 15$.

Dendritic input was the sum of two terms: $I_{\mathrm{d}}(t) = I_{\mathrm{d}\theta}(t) + I_{\mathrm{dv}}(t)$. $I_{\mathrm{d}\theta}$ was a sinusoid depolarizing current: $I_{\mathrm{d}\theta}\theta(t) = A_{\mathrm{d}}/2\,\cos(2\pi f_\theta t) + I_{0-\mathrm{d}}$, where $f_\theta = 8$ Hz, and other parameters were $A_{\mathrm{d}} = 0.5\,\mu\mathrm{A/cm^2}$, and $I_{0-\mathrm{d}} = 1.615\,\mu\mathrm{A/cm^2}$ (Fig. 2.1-2.2) or $1.9\,\mu\mathrm{A/cm^2}$ (Fig. 2.3) or $1.78\,\mu\mathrm{A/cm^2}$ (Fig. 2.4-2.5), unless otherwise noted. I_{dv} was a current proportional to the variable that was to be integrated by dendritic dynamics. This variable was $v(t)$, the running speed of the rat within the place field of the cell in Figures 2.4-2.5: $I_{\mathrm{dv}}(t) = k_{\mathrm{d}}v(t)$, where $k_{\mathrm{d}} = 0.024\ (\mu\mathrm{A/cm^2})\ /\ (\mathrm{cm/sec})$.

Somatic input was also a sum of two terms: $I_{\mathrm{s}}(t) = I_{\mathrm{s}\theta}(t) + I_{\mathrm{sv}}(t)$. $I_{\mathrm{s}\theta}$ was a sinusoid current oscillating with theta frequency in antiphase with the dendritic sinusoid input: $I_{\mathrm{s}\theta}(t) = A_{\mathrm{s}}/2\,\cos(2\pi f_\theta t + \pi) + I_{0-\mathrm{s}}$, where $A_{\mathrm{s}} = 5\,\mu\mathrm{A/cm^2}$, and $I_{0-\mathrm{s}} = -3.5\,\mu\mathrm{A/cm^2}$ (Fig. 2.3) or $I_{0-\mathrm{s}} = -4.9\,\mu\mathrm{A/cm^2}$ (Fig. 2.4-2.5), unless otherwise noted. I_{sv} was a current proportional to the variable to be encoded in somatic firing rate. This variable was again the running speed of the rat within the place field of the cell in Figures 2.4-2.5: $I_{\mathrm{sv}}(t) = k_{\mathrm{s}}v(t)$, where $k_{\mathrm{s}} = 0.1\ (\mu\mathrm{A/cm^2})\ /\ (\mathrm{cm/sec})$.

For Figures 2.4-2.5, a total of 50 traversals of the place field were simulated. In each lap, a random running speed profile was generated by choosing a different speed for the rat between 10 and $30\,\mathrm{cm/sec}$ with a uniform distribution after every $100\,\mathrm{msec}$. In order to ensure that the rat could enter the place field at any phase of theta, the time of the first speed change was randomly chosen from the $[0, 100\,\mathrm{msec}]$ interval with a uniform distribution. Finally, speed profiles were smoothed with a Gaussian kernel of 0 mean and $100\,\mathrm{msec}$ standard deviation, and position was calculated as the time-integral of the respective speed profile. For Figure 2.5, 'fast' and 'slow' runs were chosen to be the fastest and slowest 15 runs based on average running speed within the place field. Moving direction of the animal was always from left to right (Figs. 2.4 and 2.5).

2.3 Results

2.3.1 Dendritic spiking

We used a biophysical conductance-based model composed of a dendritic and a somatic compartment to investigate the integration of inputs in pyramidal cells. The dendritic compartment contained active currents that enabled it to generate slow Ca^{2+} spikes in response to sufficiently strong depolarization (Fig. 2.1A, gray line). The frequency current (f-I) curve of the dendrite showing the frequency of dendritic spiking as a function of the amplitude of tonic depolarization exhibited clear Type-I behavior (Ermentrout, 1996): as depolarization exceeded the threshold for spike generation, spiking frequency increased monotonically from $0\,\mathrm{Hz}$.

Superimposing a small oscillatory component on the tonic depolarizing current (the DC component) changed the f-I relationship substantially (Fig. 2.1A, black line) resulting in three qualitatively different regimes of dendritic dynamics. Below spiking threshold no dendritic spikes were generated (regime I). The spiking threshold was decreased, and above it the f-I curve quickly became flat over a range of depolarization strengths (regime II). In this regime, dendritic spiking frequency was determined by the frequency of the oscillatory component of external stimulation and was independent of the DC component. As further depolarization exceeded a second threshold, the integration threshold, it led to increasing spiking frequency which was primarily determined by the DC component of external stimulation as the f-I curve quickly became overlapping with that recorded in response to non-oscillatory stimulation (regime III).

Frequency-modulated oscillations integrate inputs in their phase: as long as the frequency is an approximately linear function of the input, the phase of the oscillation will be the time-integral of the input (Lengyel et al., 2003). To demonstrate this, we injected a strong depolarizing current into the dendrite that elicited periodic dendritic spiking at about $8\,\mathrm{Hz}$ (Fig. 2.1B). A short perturbating pulse current on top of this depolarization caused a phase shift in the dendritic oscillation (Fig. 2.1Ba). The amount of the phase shift depended on the phase of the dendritic oscillation at which the perturbating current was delivered: perturbation was only effective in the second half of the spiking cycle (Fig. 2.1Ca). Moreover, the size of the phase shift was linear in the amplitude of the perturbating current within a range of pulse

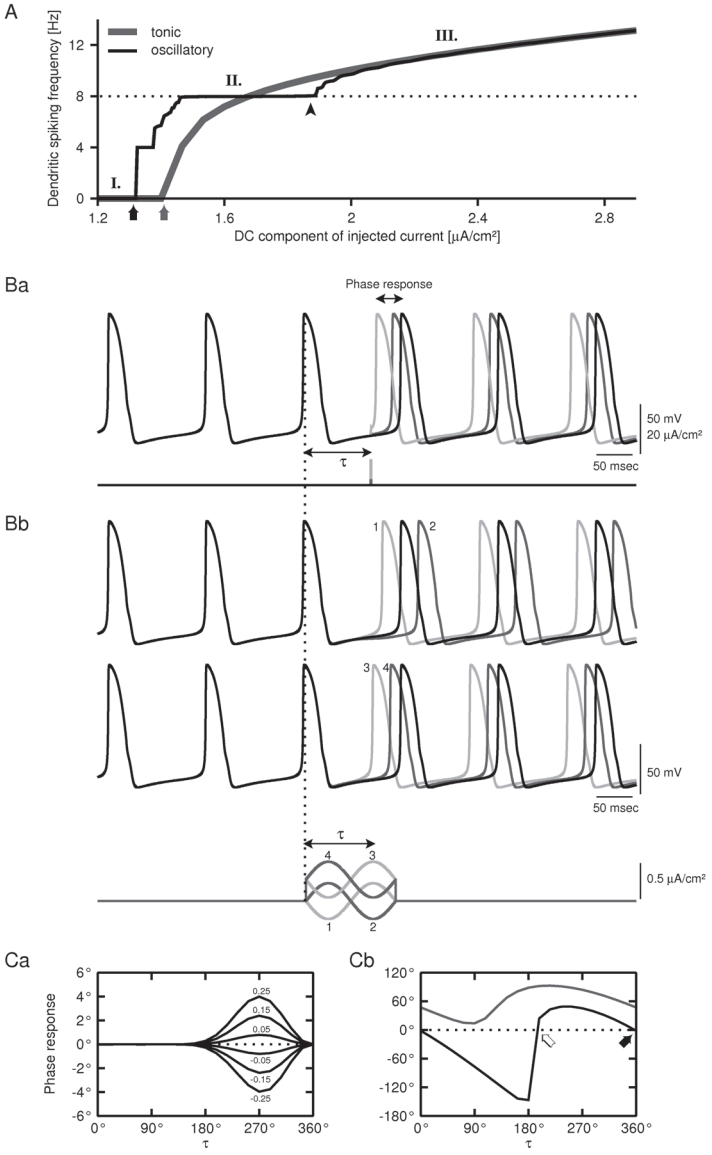
A
tonic
oscillatory
Dendritic spiking frequency [Hz]
12
8
4
0
I.
II.
III.
1.2
1.6
2
2.4
2.8
DC component of injected current [μA/cm²]
Ba
Phase response
τ
50 mV
20 μA/cm²
50 msec
Bb
1
2
3
4
50 mV
50 msec
τ
0.5 μA/cm²
Ca
Phase response
6°
4°
2°
0°
-2°
-4°
-6°
0.25
0.15
0.05
-0.05
-0.15
-0.25
0°
90°
180°
270°
360°
τ
Cb
120°
60°
0°
-60°
-120°
-180°
0°
90°
180°
270°
360°
τ

Figure 2.1: **Characteristics of periodic dendritic spiking induced by constant and oscillatory stimulation. A**. Spiking frequency of the dendritic compartment as a function of the DC component of injected current (f-I curve). Above firing threshold (*gray arrow*), tonic stimulation (*thick gray line*) resulted in increasing spiking frequencies. Oscillatory stimulation (*thin black line*) resulted in a decreased spiking threshold (*black arrow*, regime I) and frequency locking to the oscillatory input (*dotted line*) in a wide range of the DC component (regime II). Above integration threshold (*black arrowhead*, see text), the frequency of dendritic firing quickly converged to the tonic depolarization-induced f-I curve (regime III). **B.** Phase responses of the dendritic oscillation to transient stimulation. **Ba.** Illustration of the stimulation protocol. Constant stimulation (*lower black line*) caused periodic spiking in the dendrite of the pyramidal cell model (*upper black trace*). A $1\,\mathrm{msec}$ pulse current superimposed on the constant depolarization (*lower gray line*) induced a shift in dendritic spiking (*upper light gray trace*). This *phase response* depended on the timing of the pulse relative to the spiking cycle (τ, *light* and *dark gray* membrane potential traces). Note that both the phase response and τ are measured in degrees relative to the dendritic inter-spike interval (ISI). **Bb.** Phase responses of the dendrite resulting from periodic stimulation. A single cycle of sinusoid current with a given offset and phase superimposed on the tonic stimulation (*lower panel*) caused either both delay and advance of dendritic spiking (*upper panel*) or only advance (*middle panel*), depending on stimulus offset. *Upper and middle panel*: *black traces* are dendritic membrane potentials with tonic stimulation, *gray traces* correspond to dendritic membrane potentials resulting from transient periodic stimulation. Labels and colors correspond to those used in the *lower panel*. Note, that here τ denotes the time of the peak of the oscillatory component relative to the ongoing dendritic oscillation. **C.** Phase response curves of the dendritic compartment as a result of current pulse stimulation (subfigure Ca) and oscillatory stimulation (subfigure Cb). Positive phase response means advance (shorter ISI), negative means delay (longer ISI). **Ca**. Current pulse stimulation with positive pulse-amplitudes (*positive labels*) resulted in strictly positive phase response curves. Phase response curves scaled linearly with pulse amplitude (labels denote pulse amplitudes in $\mu\mathrm{A}/\mathrm{cm}^2$). **Cb**. Oscillatory phase response curves (oPRCs), calculated with the protocol illustrated on subfigure Bb, at different offset currents ($0\,\mu\mathrm{A}/\mathrm{cm}^2$ and $0.3\mu\mathrm{A}/\mathrm{cm}^2$ for the *black* and *gray lines*, respectively). While at low offset-levels both positive and negative phase shifts could be achieved, causing advanced or delayed spiking (*black line*), at high offset levels only positive phase shifts were available (*gray line*). At zero-crossing a stable (*black arrow*) and an unstable fixed point (*white arrow*) are present depending on the slope of the oPRC. At high offset-levels no fixed points are present causing a continuous shift in the phase of spiking. Note, that the *black curve* corresponds to regime II , while the *gray curve* corresponds to regime III of the f-I curve (subfigure A).

amplitudes (Fig. 2.1Ca).

To analyze the effect of an oscillatory current injection, a full cycle of sine wave stimulus was applied on top of the baseline stimulus with different starting phases and offset values (Fig. 2.1Bb). Oscillatory inputs with small offsets could both advance or delay the next dendritic spike depending on the starting phase of the stimulation (Fig. 2.1Bb, upper trace). Spiking was advanced when the dendritic spike lagged behind the peak of the sine wave stimulus, and delayed when the dendritic spike occurred before the peak of the sine wave stimulus (Fig. 2.1Cb, black line).

This means that applying the same oscillatory current for several cycles drives dendritic spiking so that it becomes phase locked to this external oscillation. As long as the oscillatory phase-response curve (oPRC) crosses zero with a negative slope there is a stable phase lag for dendritic spiking (a crossing with positive slope indicates an unstable phase lag), and thus its frequency is kept at the frequency of the external stimulation (regime II of the f-I curve, Fig. 2.1A). Oscillatory current injection with an elevated offset could only cause spike advance (Fig. 2.1B, lower trace) shifting the oPRC above zero at all phase lags (Fig. 2.1Cb, gray line), as it amounted to an overall excitation above the integration threshold (regime III of the f-I curve, Fig. 2.1A).

We compared the integrative properties of two dynamical modes of the dendritic membrane. Without strong baseline depolarization, the dendrite integrated inputs in its membrane potential (Fig. 2.2A) as determined by its passive properties (Rall, 1959). Long time scale integration in this mode was hampered in two ways. First, the membrane potential became quickly saturated for long inputs, instead of increasing linearly with stimulus length. Second, after the cessation of the stimulus the membrane potential returned to its resting value within tens of milliseconds (Fig. 2.2Aa), instead of staying constant. The rate of this decay and therefore the time constant of integration was determined by the membrane time constant (Fig. 2.2Ab).

Strong oscillatory baseline stimulation (regime II) elicited periodic dendritic spiking and the phase precession of dendritic spiking was roughly proportional to the length of dendritic stimulation above the integration threshold (Fig. 2.2Ba). The slight curvature in the phase shift curve was attributable to the sinusoid shape of the oPRC (Fig. 2.1Cb, gray line): its distance from the zero axis was uneven, and therefore phase shifts were bigger or smaller when dendritic spiking lagged or led the peak of the external oscillation, respectively. In the absence of extra stimulation, the oscillatory component of baseline stimulation drove dendritic spiking back to the stable phase lag shown in Figure 2.1Cb in a few theta cyles. However the speed of this decay could be slowed down dramatically by decreasing the amplitude of the oscillatory component to the input (Fig. 2.2Bb). As spiking phase is a circular variable, decay back to baseline phase could occur in one of two ways. It occurred either through phase precession or through phase recession, depending on what the spiking phase was at the end of stimulation (Fig. 2.2C), just as predicted by the oPRC of the dendritic membrane (Fig. 2.1Cb). In summary, in the periodically

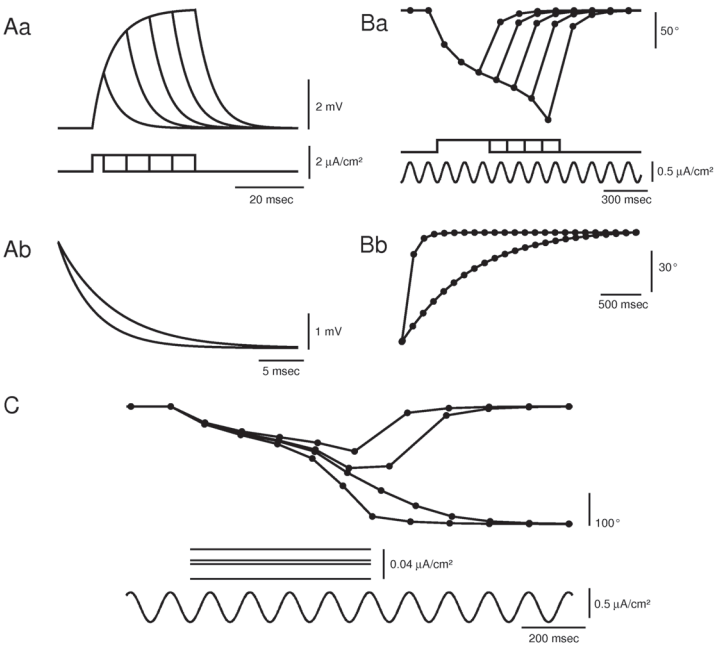

Figure 2.2: **Comparison of input integration in dendritic membrane potential and in the phase of dendritic spiking. A.** Below spiking threshold, current pulses of increasing length (**Aa**, *lower traces*) induced saturating membrane potential changes. Time scale of the integration process was determined by the membrane time constant (**Ab** ($4\,\mathrm{ms}$ and $2.86\,\mathrm{ms}$ for the *upper* and *lower trace*, respectively). **B.** Above integration threshold, current pulses (**Ba**, *middle traces*) induced the advancement of dendritic spiking (*upper traces*) relative to the periodic stimulation (*lower trace*). Total amount of phase precession increased monotonously and without saturation as the length of stimulation was increased. Phase of dendritic firing settled to the stable phase after stimulation returned to baseline level (regime II). Time course of decay dynamics of dendritic spiking-phase (**Bb**) was determined by the amplitude of the oscillatory component ($0.5\,\mu\mathrm{A/cm^2}$, and $0.05\,\mu\mathrm{A/cm^2}$ for the *upper* and *lower* trace, respectively). Note the difference between the scale bars in subfigures A and B indicating the difference of the integration time scale in the two cases. **C**. After cessation of stimulation, phase of dendritic spiking relative to the periodic stimulation component settled to the stable phase either by advancing spiking phase (*upper panel*, *lower two traces*) or by delaying it (*upper panel*, *upper two traces*). Whether phase precession or phase recession occurred depended on the spiking phase at the end of regime III stimulation. Here, different exit phases were achieved by slight changes in the DC components (*middle panel*, duration of the simulation corresponds to the extent of the lines, and DC levels correspond to respective traces of the *upper panel* in a reversed order).

spiking regime, the dendrite integrated inputs above the integration threshold near-perfectly, and behaved as a leaky integrator with a time constant much longer than its membrane time constant for inputs below this threshold.

2.3.2 Somatic firing

The somatic compartment of the model cell contained currents for firing fast Na^+ action potentials. In response to a subthreshold theta-frequency current injection its membrane potential went through periodic cycles of de- and hyperpolarization. This provided a straightforward read-out mechanism for the phase code of dendritic spiking (Fig. 2.3).

If the dendrite spiked in the hyperpolarized phase of the soma, the dendritic spike could not invade and no somatic action potentials were fired. However, the more the dendritic spike overlapped with somatic depolarization, the more action potentials the soma could fire. This resulted in doubly coded somatic firing (Lengyel et al., 2003): dendritic spiking phase was reflected both in the phase of somatic spikes and the number of spikes during a theta cycle (Fig. 2.3A).

The DC component of somatic input could decouple the phase and rate code of somatic firing (Fig. 2.3A, gray lines). Firing phase was largely unaffected by increasing DC somatic input as it was still determined by the timing of dendritic spikes, while firing rate increased because depolarization of the somatic membrane between consecutive action potentials was accelerated.

As the sinusoid components of dendritic and somatic inputs were set to be in antiphase, and dendritic spikes were phase locked to the dendritic oscillation at baseline (Figs. 2.1Cb and 2.2Ba), somatic firing rate was low without extra excitation (Fig. 2.3B). When the input current exceeded the integration threshold dendritic spikes began to phase shift, thus becoming increasingly in phase with somatic depolarization and resulting in an increasing number of somatic action potentials. As phase precession of dendritic spiking continued due to sustained input, dendritic spikes became out-of-phase with somatic depolarization and somatic firing rate decreased accordingly. This periodic waxing and waning of somatic firing rate could continue as long as dendritic input was present (data not shown).

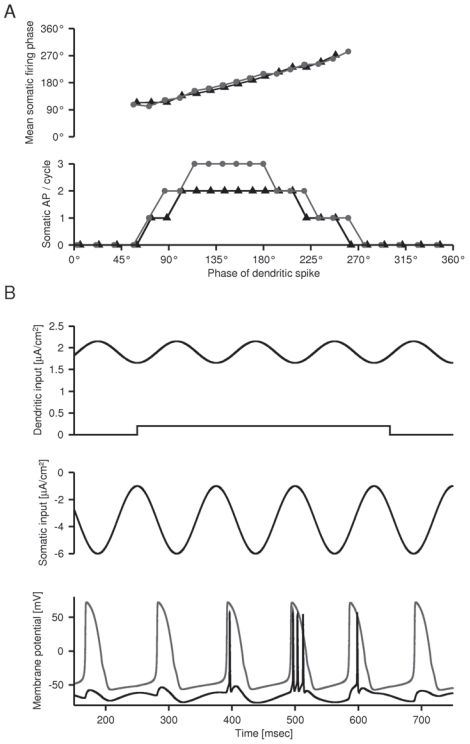

Figure 2.3: **Somatic read-out of dendritic integration. A.** DC component of somatic stimulation did not affect the mean phase of somatic action potentials (*upper panel*), but had a significant effect on the number of somatic action potentials fired per oscillation cycle (*lower panel*): increased DC components resulted in higher number of action potentials per cycle. DC components were $-3.5\,\mu\mathrm{A}/\mathrm{cm}^2$ and $-4\,\mu\mathrm{A}/\mathrm{cm}^2$ for the *gray* and *black* symbols, respectively. Zero degree corresponds to the phase of strongest somatic hyperpolarization here and hereafter. **B**. Phase precession of action potentials. Hyperpolarizing subthreshold oscillatory input delivered to the soma (*middle panel*) was set anti-phase with the oscillatory component of the dendritic stimulation (*upper panel*, *upper trace*). When DC dendritic input (*upper panel, middle trace*) was below integration threshold dendritic spiking was phase locked to the oscillatory component of dendritic input. As a result of the anti-phasic relationship, dendritic spiking could not elicit somatic action potentials (first $300\,\mathrm{ms}$ in the plot). Pushing the dendrite over the integration threshold by a small current pulse, dendritic spiking precessed, thus the overlap between dendritic spiking and somatic oscillatory increased. At the same time, number of somatic action potentials increased up to the maximum overlap and decreased again as the dendritic spikes were generated earlier than the maximum of the somatic input.

2.3.3 Comparison with place cell data

Pyramidal cells of the hippocampus are known to exhibit location-specific firing in the behaving rat: a 'place cell' only fires when the rat is in a circumscribed region of the environment, the 'place field' of the cell (O'Keefe and Dostrovsky, 1971). Place cell recordings thus provide detailed quantitative *in vivo* data on the firing patterns of hippocampal pyramidal cells against which we tested the predictions of our model.

As suggested by earlier modeling (Lengyel et al., 2003; Lengyel and Érdi, 2004), we took dendritic input to be proportional to the running speed of the animal. Because position is the time-integral of velocity, the phase of dendritic spiking became proportional with the position of the animal as it kept integrating running speed. The somatic read-out mechanism (Fig. 2.3) thus ensured that both firing rate and firing phase of somatic action potentials coded for the position of the animal. In line with earlier modeling studies using abstract models (Lengyel et al., 2003), this produced a unimodal firing rate tuning curve, and a monotonically decreasing phase precession curve spanning a full cycle of theta oscillation (Fig. 2.4A), where firing phase was more correlated with position than with time spent in the place field (Fig. 2.4B), just as seen in experiments (O'Keefe and Recce, 1993; Huxter et al., 2003).

However, overall phase shift of place cells always amounts to an integer number of theta cycles (usually just a single theta cycle) (O'Keefe and Recce, 1993; Skaggs et al., 1996). This may not seem to be reproduced by our model unless the integral of dendritic input is exactly matched so that dendritic spiking is ensured to precess an integer number of theta cycles. Furthermore, if phase precession does not stop after spanning a full cycle of theta oscillation, the model predicts sustained firing after the animal leaves the place field of the cell. Contrary to these inauspicious expectations, the model stopped firing even when the integral of dendritic input was not exactly matched to produce one cycle of dendritic phase precession (Fig. 2.4C). This happened because after the cessation of input, free-running phase shift drove dendritic spiking back to the stable baseline firing phase at which it was phase locked to the dendritic oscillation (Figs. 2.1Cb and 2.2C) and therefore could not evoke somatic firing (Fig. 2.3). Such an inertia-like behavior of place cell firing was observed in experiments when rats were made to turn around before reaching the end of a place field (Redish et al., 2000). As changes in firing phase are determined by the internal dynamics of the dendrite during free-running phase

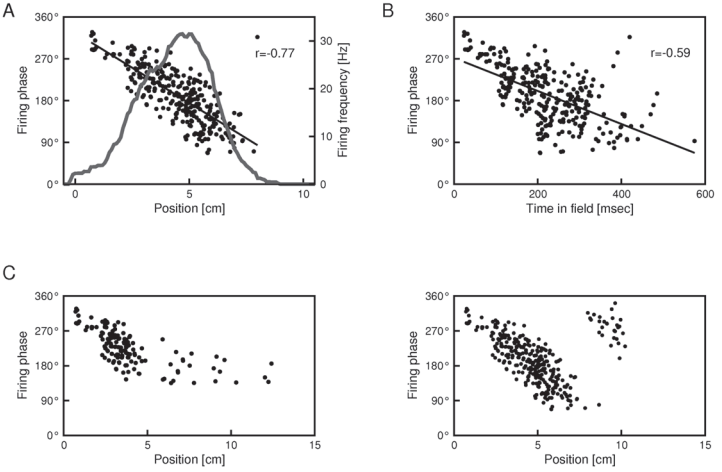

Figure 2.4: **Rate and phase coding in place cells as reproduced by the model. A.** While phase of somatic firing (*black dots*) is a monotonically decreasing function of position, the firing rate has a unimodal profile (*gray line*). Comparison of firing phase data plotted against position (**A**) and that plotted against the time spent in the place field (**B**) reveals a higher correlation (r) with position than with time. *Black lines* are regression lines fitted on data points. Aggregate data from multiple traversals of the place field is presented, where speed of the animal was subject to change both during a single traversal and across traversals. **C**. Phase precession did not require precise tuning of place field size: whether the phase precession was less than a full cycle of theta oscillation (*left panel*) or was longer than a cycle (*right panel*) the place cell ceased to fire action potentials shortly after leaving the place field.

shift, this mechanism also predicts a smaller correlation between firing phase and position of the animal in the second half of the place field than in the first half. A decline in correlations between firing phase and position within the place field was also demonstrated in experiments (Mehta et al., 2002; Yamaguchi et al., 2002).

Our two compartmental model also predicted that the DC component of the somatic input should modulate the firing rate of the cell while leaving firing phases relatively unaffected (Fig. 2.3A). If this somatic input is proportional to the running speed of the animal this results in a specific decoupling of the rate and phase code of place cells (Fig. 2.5). Faster runs through the same place field should be associated with higher firing rates, while the firing phase-position relationship should not show any systematic changes (Fig. 2.5A and B). Indeed, such a decoupling of firing phase and rate has been found in place cells (Huxter et al., 2003), and the relative magnitude of correlation coefficients found in experiments were well matched by the predictions of our model (Fig. 2.5C). Thus the two compartmental mechanism proposed here was capable of encoding (the integral of) one variable in the firing phase of the neuron, while modulating its firing rate depending on a second variable.

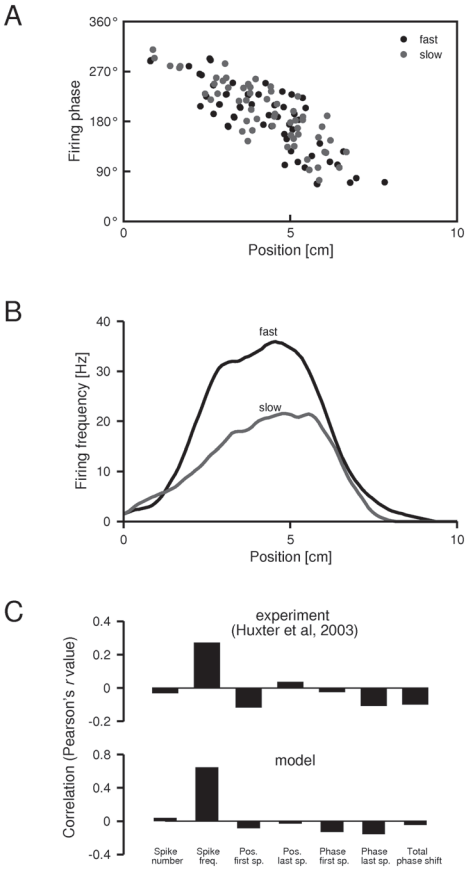

Figure 2.5: **Decoupling the rate and phase code.** Firing phase data collected from fast (**A**, *black*) and slow (*gray*) place field traversals had an overlapping profile. Firing rate tuning curves (**B**), however, were significantly different, faster runs peaking at higher levels than slower runs. **C**. Analysis of the running speed-dependence of the rate and phase code. Correlation coefficients between running speed and various characteristics of place cell firing were calculated (*lower panel*). Labels denote number of spikes fired in the place field (*spike number*), average firing frequency (*spike freq.*), position of the animal in the place field when the first (*pos. first sp.*) and last (*pos. last sp.*) spike was fired, phase of the first (*phase first sp.*) and last (*phase last sp.*) spike relative to theta oscillation, and the *total phase shift* in the place field. The most significant correlation was measured between running speed and average firing frequency. Data obtained from simulations and experiments (*upper panel*, Huxter et al., 2003) were closely matching.

2.4 Discussion

2.4.1 Plausibility of periodic dendritic spiking

Dendritic spikes are traditionally considered to be the final outcomes of dendritic integration: they signal that net local input to the dendrite exceeds a given threshold (the spike generation threshold) (Williams and Stuart, 2003). We propose that periodic dendritic spikes convey information by the change in their timing rather than by their appearance *per se*. A similar scenario has been suggested earlier (Marder et al., 1996) for somatic firing, but because periodic firing is a prerequisite for this type of coding, constant firing rates had to be assumed. This does not seem to be consistent with the firing pattern of cortical pyramidal cells undergoing substantial firing rate modulations (Major and Tank, 2004). In our model, although the dendrite regularly generates spikes, somatic action potentials are only triggered when a dendritic spike coincides with somatic depolarization, thereby resulting in systematically varying somatic firing rates (Figs. 2.3, 2.4).

The mechanism for dendritic spike generation in our model is admittedly simplified: it is an interplay of a low-threshold non-inactivating Ca^{2+} current, and a Ca^{2+}- and voltage-dependent K^+ current (Pinsky and Rinzel, 1994). Pyramidal cell dendrites possess a much richer repertoire of voltage-gated channels, and therefore exhibit more complex dynamics than that demonstrated here (Magee et al., 1998; Hausser et al., 2000; Reyes, 2001). Nevertheless, we expect the main findings of our work to apply as long as dendrites are shown to be able to behave as type I oscillators (Fig. 2.1). Periodic Ca^{2+} spikes in pyramidal cell dendrites during hippocampal theta oscillations were observed *in vitro* (Gillies et al., 2002) and *in vivo* (Kamondi et al., 1998), and the frequency of dendritic oscillations could be modulated by the amount of depolarization (Kamondi et al., 1998), in line with the predictions of the model (Fig. 2.1). However, whether these suprathreshold oscillations are of type I remains to be tested, as there have yet been no systematic studies on the f-I curves or PRCs of pyramidal cell dendrites.

The amplitude of experimentally observable dendritic spikes also tends to be smaller (around $10\,\mathrm{mV}$, Kamondi et al., 1998; Gillies et al., 2002) than that of the full-blown Ca^{2+} spikes seen in the model (Fig. 2.1B, 2.3B). This is important, because these spikes may then not be able to propagate to the soma and ever elicit somatic ac-

tion potentials, thus undermining a crucial assumption of our model. Yet, in other studies, dendritic spikes were shown to actively propagate towards the soma and trigger fast action potentials there under *in vivo*-like conditions (Williams, 2004). It is not clear what causes this discrepancy in experimental findings. One possibility is that the amplitude of dendritic spikes appeared smaller in some experiments (Kamondi et al., 1998; Gillies et al., 2002) because they were not recorded at the site of their generation. This also raises an interesting issue about how multiple potential spike generating compartments may interact in the same dendritic tree, or how dendritic morphology may influence the propagation of dendritic spikes (Vetter et al., 2001). Models with more detailed morphology than the extremely simplified two-compartmental structure used here will be needed for studying such interactions.

2.4.2 Firing patterns indicative of theta oscillation-coupled long time-scale integration in behaving animals

Current experimental techniques do not yet permit routine dendritic recordings in freely behaving animals, although they may soon become available (Helmchen et al., 2001). We used data from place cell recordings to test whether the neural firing patterns seen in exploring rats are consistent with our proposed dendritic integration mechanism (Fig. 2.4, 2.5). We found that even fine details of place cell firing were accounted for by the model, such as relative correlations between firing phase and position (Fig. 2.4A and C) or time spent in the place field (Fig. 2.4B) (O'Keefe and Recce, 1993; Huxter et al., 2003), and between running speed and various quantitative characteristics of firing (Fig. 2.5) (Huxter et al., 2003). This is also consistent with several earlier proposals that the hippocampus and surrounding areas may be involved in path integration (McNaughton et al., 1996; Redish and Touretzky, 1997; Samsonovich and McNaughton, 1997; Sharp, 1997). However, a recent study by Zugaro et al. (2005) showed that hippocampal cells continued phase precessing after transient intrahippocampal perturbation that otherwise seemed to disrupt hippocampal theta activity. This is inconsistent with simple integration models like the one presented here (O'Keefe and Recce, 1993; Lengyel et al., 2003), and points to alternative or at least additional mechanisms for explaining place cell firing (Tsodyks et al., 1996; Jensen and Lisman, 1996; Wallenstein and Hasselmo, 1997; Mehta et al., 2002; Yamaguchi, 2003).

Persistent activity of putative pyramidal cells in the hippocampus was also observed during the delay period of a delayed non-match-to-sample (DNMS) task (Deadwyler and Hampson, 2004). Although field potentials were not recorded in these experiments, other studies had found hippocampal theta activity while animals performed tasks similar to these (Givens and Olton, 1990; Givens, 1996). Hence, our model predicts that if the ramping activity seen in these cells is really generated within the hippocampus and not transmitted from upstream areas, these cells should also show gradual phase precession during the delay period.

In a recent study, Lee et al. (2005) recorded neurons in monkey extrastriate visual cortex during a working memory task. They also found a significant enhancement of theta oscillations during the delay period, where theta power was shown to be directly related to the memory component of the task and not to other non-specific effects. Several neurons showed elevated firing rates during the same period, and most importantly, their firing rate and phase strongly covaried (cf. our Fig. 2.3A). Moreover, the preferred phase of firing was very similar across neurons. These data are highly consistent with the behavior of our model.

2.4.3 The role of theta oscillations

Three aspects of theta oscillations are essential for the integration mechanism of our model. (1) The dendritic membrane has to be depolarized sufficiently over the spike generation threshold, so that dendritic spikes can integrate inputs in their timing (Fig. 2.1). In line with this, the dendritic membrane of hippocampal pyramidal cells was found to be depolarized during theta oscillations, and to spontaneously generate spikes with theta frequency (Kamondi et al., 1998, and see above). (2) Depolarization of the dendritic membrane needs to have a periodic component with theta frequency so that there is a threshold (the integration threshold, Fig. 2.1) under which noisy inputs do not influence dendritic integration. The oscillatory dendritic input also serves as a reference signal against which the timing of dendritic spikes can be 'measured'. Pyramidal cell dendrites also showed subthreshold theta frequency oscillations, and dendritic spikes rode on the peaks of these oscillations (Kamondi et al., 1998), just as predicted by the model under baseline conditions (Figs. 2.1Cb, 2.2B and C, and 2.3B). (3) The somatic membrane needs to be periodically hyperpolarized with the same frequency so that somatic action potentials are fired depending on the relative phase of dendritic spikes. The somatic and den-

dritic oscillations have to be in antiphase so that the cell fires minimally under baseline conditions (Fig. 2.3). Hyperpolarizing somatic membrane potential oscillations have been described in pyramidal cells during theta, and these oscillations were in antiphase with the dendritic oscillation (Kamondi et al., 1998; Gillies et al., 2002).

Thus it seems that all conditions are provided for our model to perform long time scale-integration – at least in the hippocampus. In particular, the activity of different subclasses of interneurons specifically innervating different regions of the denritic trees of pyramidal cells (Freund and Buzsáki, 1996), as well as the input from the entorhinal cortex are strongly theta modulated (Csicsvári et al., 1999; Frank et al., 2001; Klausberger et al., 2003) and their preferred firing phases support the specific theta-related effects required by our theory. Yet, integration on long time scales was observed in several brain areas (Major and Tank, 2004) and was suggested to serve a number of purposes from stabilizing eye position (Seung, 1996) to integrating evidence for decision making (Gold and Shadlen, 2002). Whether theta oscillations satisfy the above conditions in brain regions other than the hippocampus remains to be tested.

It is nevertheless suggestive that short term memory tasks are often accompanied by theta oscillations (Kahana et al., 2001; Jensen and Lisman, 2005), and the presence of theta oscillations was shown to be necessary for successful performance in these tasks (Winson, 1978; Givens and Olton, 1990; Mizumori et al., 1990; Pan and McNaughton, 1997). Other models have been proposed to account for this (Lisman and Idiart, 1995; Jensen and Lisman, 1998), but they predict relatively constant firing rates within trials, while our model accommodates time-varying firing rates, such as the ramping behavior often seen in these experiments (Brody et al., 2003; Baeg et al., 2003; Deadwyler and Hampson, 2004). As the sensitivity of the dendritic membrane to inputs in our model depends on the phase at which the input arrives (Fig. 2.1C), the timing of inputs has a profound effect on the efficacy of dendritic integration. This may also offer some insight into why different brain areas show synchronization and an increase in coherency in the theta band during short term memory tasks (Macrides et al., 1982; Sarnthein et al., 1998; Stam et al., 2002; Fell et al., 2003; Seidenbecher et al., 2003; Mizuhara et al., 2004; Sauseng et al., 2004).

3

Distance representation

3.1 Introduction

Behavioral experiments have shown that rodents (Siegrist et al., 2003), cats (Poucet et al., 1983) and chimpanzees (Menzel, 1973) are able to learn the layout of their environment, make detours and find shortcuts if they face obstacles or have to cross unknown areas while they navigate. To achieve these metric navigation tasks, the animal has to possess metric information i.e. distance among places and direction from specific points in the environment. Orientation of the animal is encoded by head direction cells that were first discovered in the dorsal presubiculum (Ranck, 1984) but was later found in many other brain regions, including thalamus (Taube, 1995), mammillary nucleus (Stackman and Taube, 1998), retrosplenial cortex (Chen et al., 1994), striatum (Wiener, 1993) and layer III of the entorhinal cortex (Sargolini et al., 2006). However, neurons representing distance from specific points have not been described yet.

The majority of principal cells in the hippocampus are place cells that show spatially correlated activity, representing specific positions of the environment. In the CA3 region of the hippocampus, there is a significant number of lateral cross connections between principal cells, therefore a natural assumption of computational models (Trullier and Meyer, 2000) was that the connection strengths between CA3 place cells could represent distances between positions. However, place cells are not topographically organized, they randomly remap in a new environment, therefore distance between positions represented by any two place cells is not constant, it depends on the environment. This makes hard to implement metrics by the CA3 recurrent collaterals, since the connection strengths in the whole connection system should be reorganized in each environment for correct distance representation.

The attention has been recently drawn to the medial entorhinal cortex (MEC) layer

II pyramidal cells (Fyhn et al., 2004; Hafting et al., 2005; Sargolini et al., 2006; Fyhn et al., 2007; Moser et al., 2008) that show a topographic organization. These *grid cells* were shown to be active on the vertices of triangular grids tessellating the plane and each cell is characterized by the spacing (spatial periodicity), orientation and the 2 dimensional phase value of its grid (Fig. 3.4 C). The cells were found to be topographically organized along the dorsoventral axis of MEC according to their spacing value. This grid cell system is considered as an explicit example of metric space representation in the central nervous system (Jeffery and Burgess, 2006; Moser et al., 2008) and according to the present view, the function of grid cell system is to perform path integration (Fuhs and Touretzky, 2006; Guanella et al., 2007). These properties make the grid cell system a possible source of metric information.

However, due to the periodic nature of their spatial code, extraction of distance information from these cells is not straightforward, further computations are necessary to perform this task. First (Section 3.2) we propose three models for distance representation in the nervous system: the first two models execute distance estimation without the grid cell system while in the third model distance information is extracted from the activity of grid cells (*grid model*). We calculate and compare the number of cells and the extent of average firing activity necessary for exact distance representation in case of the three distance estimating models and conclude that the grid model achieves the most effective distance coding mechanism. Second (Section 3.3), functioning of the distance estimating system is demonstrated by numerical simulations of the grid model. Distance of the animal from significant places is encoded by the population activity of hypothesized *distance cells* that receive input both directly and indirectly (through inhibitory cells) from the grid cell system. We study two variants of the general model: in one of them, the direct input is dominant, while in the other one it is negligible and distance cell activity is mainly determined by the indirect input. Distance coding capabilities and the estimation precision of the two model variants are analyzed and prediction is given for the firing pattern of the proposed distance cells.

3.2 Analysis of distance representing neural networks

3.2.1 Model

Each model is a feed-forward two-layered neural network, in which the 'pre-distance cell' (pre-DC) layer represent certain locations in the environment while the 'distance cell (DC)' layer receives innervation from pre-distance cells (Fig. 3.1 A, B, C) and represents the distance of the animal from a significant location (let us denote it as origin). The three models differ only in the properties of pre-DCs:

1. *Place-pair model*: pre-DCs are excited at two different locations, thus have two receptive fields in the environment (Fig. 3.1 A). The cell is firing when the rat occupies any of these locations.

2. *Triangle model*: one pre-DC represents the set of places where the all-to-all distances are identical. The maximal number of places fulfilling this requirement is only 3 and these places are located on the vertices of an equilateral triangle (Fig. 3.1 B).

3. *Grid model*: a pre-DC in this model represents a group of places in the environment, where the pairwise distances between places are equal or larger than a given S distance (Fig. 3.1 C). The densest packing of such places forms a triangular lattice with spatial periodicity S, similar to a receptive field of an entorhinal grid cell with spacing S.

In each model, the projection from layer I to layer II is convergent so that each DC is innervated by all the pre-DCs that share a common receptive field distance. This distance value will be represented by the DC. We assume that the following one-shot learning mechanism takes place when the animal occupies the origin: synapses between pre-DCs having receptive field at the origin and postsynaptic DCs innervated by them get long-term potentiated (Fig. 3.1 D, thick arrows) and these synaptic weights become proportional to the firing frequency of the pre-DC in the origin (this equals to Hebbian learning if firing activity of different DCs is assumed to be equal in the origin). After leaving the origin, the most active DC in any position will be the one that receives excitation on its strengthened, potentiated synapse, thus from pre-DC having one of its receptive fields at the origin and the other at the animal's actual position (Fig. 3.1 E). Distance between these receptive fields naturally

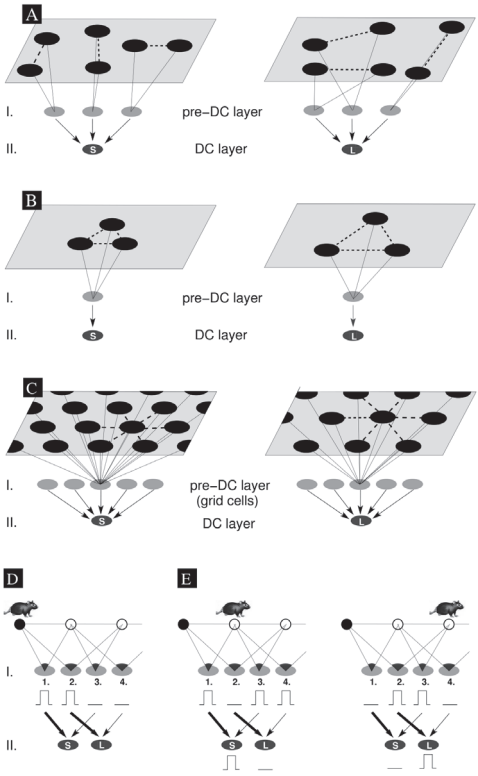

Figure 3.1: **Schema of different possibilities for distance estimation.** Cells are represented by grey circles and the receptive fields of the cells are depicted by black circles **A.** Place-pair model. Each pair of places are represented by a pre-distance cell (pre-DC). All the pre-DCs with the same distance among theirs receptive field pairs project to the same distance cell (DC), encoding the given - shorter (S) or longer (L) - distance. **B.** Triangle model. The number of the required pre-DCs can be reduced by representing all the places with the same pairwise distance by only one pre-DC. These places are located on the vertices of equilateral triangles (black circles). **C.** Grid model. All the places where pairwise distances are equal or larger than a given value (vertices of a triangular lattice) are represented by one grid cell (the receptive fields of only one grid cell are shown). Grid cells with equaling spacing innervate the same DC. **D.** Setting the origin. The one-shot learning potentiates the synapses between the currently active pre-DCs and the DCs (thick arrows) and so sets the origin to the current position of the rat (black circle). **E.** Tracking the distance from the origin. Distance from the origin is represented by the active DC that receives excitation at the actual position of the rat on a previously strengthened synapse.

equals the distance of the animal from the origin. Assuming that the correspondence between distance cells and distances is stored somehow in the brain, the identity of the most active DC unambiguously encodes the distance information. This storage can be achieved for example by a structured spatial distribution of the cells similarly to that observed in the medial entorhinal cortex where the spacing value of grid cells increases monotonically along the dorso-ventral axis of the tissue. In a similar case, the location of the DC with highest firing frequency would encode the distance of the animal from the origin.

3.2.2 Results

In this section we compare the presented three different models to study how distance can be optimally encoded by a neural system. Optimality is defined in two ways: (1) by the total number of neurons in the neural network and (2) by the average firing activity of the system which is assumed to be proportional to the number of cells that are active at the same time (i.e. in the same position). Cell numbers are expressed as a function of the environment size and the estimation precision. The estimation precision is defined by the maximum of the estimation errors for distances between any two locations in the environment. Two types of errors were considered: absolute error is the difference between the real and the estimated distance value, while relative error is the fraction of this difference and the real distance. In the followings we present the result of the analytical calculations on the required total number of cells in the network and the number of cells that are simultaneously active, when the value of absolute or relative error is bounded. The number of required cells equals to the sum of the number of pre-DCs and DCs in each case. However, as the number of DCs, that is the number of represented distances, should be the same in the three different models, only the number of necessary pre-DCs (place pairs, place triplets and grids) is calculated. Precise calculations can be found in the Appendix.

Let assume that the distance estimation should work in an open, large environment where any pair of positions should be addressable by the network. In order to simplify the calculations, triangular shape of the environment is assumed, with side length L. Differences in the shape of the environment cause quantitative differences in the results, but the overall conclusions will be based on the scaling properties of different solutions, which is unaffected by the shape of the environment.

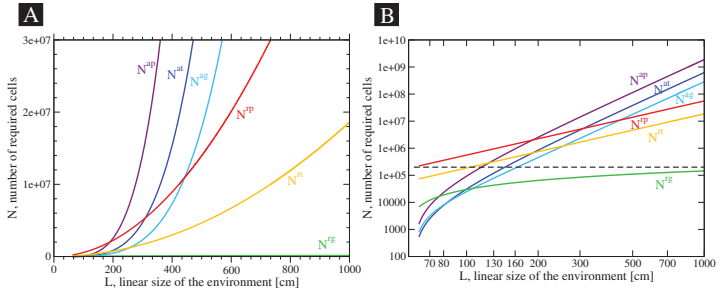

Figure 3.2: **Results on the total number of cells in linear (A) and log-log axes (B).** N^{ap}, N^{at} and N^{ag} stand for the results on the place-pair, the triangle and the grid models with bounded absolute error ($d = 3\ cm$), while N^{rp}, N^{rt} and N^{rg} denote the place-pair, the triangle and the grid models with bounded relative error ($C = 0.1$), respectively. The maximal distance to be measured was set as $D_{max} = L/2$. The estimated number of pyramidal cells in the medial entorhinal cortex is around 200000 (dashed line).

The total number of required pre-DCs (Fig. 3.2) in case of bounded absolute error is proportional to the size of the environment, it increases with the 4th power of L in all three models (Appendix A.1, A.2):

$$N^{ap}, N^{at}, N^{ag} \propto \mathcal{O}(L^4) \tag{3.1}$$

However, the coefficient is different resulting that the place-pair model needs the most, whereas the grid model needs the fewest neurons.

Although the grid model reduced the necessary number of neurons, the magnitude is the same for all three models and results in a huge number of neurons even in relatively small environments. This can be significantly reduced by weakening the strict requirement for the bounded absolute error by requiring only bounded *relative error*.

Bounding the relative error means that the estimation error divided by the distance to be estimated should remain under a given constant. With this constraint, the number of required cells is proportional to the area of the environment in case of place-pair and triangle models (Appendix A.3):

$$N^{rp}, N^{rt}, \propto \mathcal{O}(L^2) \tag{3.2}$$

In contrast, the total number of necessary cells in the grid model increases only logarithmically with the linear size of the environment (Appendix A.4):

$$N^{rg} \propto \mathcal{O}(\log(L)) \tag{3.3}$$

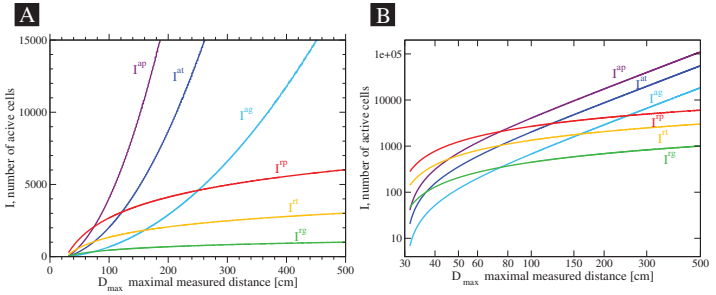

Figure 3.3: **Results on the number of simultaneously active cells on linear (A) and log-log axes (B).** Number of active cells increases quadratically with the maximal measured distance (D_{max}) in case of bounded absolute error (I^{ap}, I^{at} and I^{ag}). However, optimal solutions for relative error bound (I^{rp}, I^{rt} and I^{rg}) results in logarithmic increasing in the number or active cells.

The optimal solutions for bounded relative error uses overlapping receptive fields, thus requires more cells in small environments (Fig. 3.2 B). However, this initial difference is reversed shortly with the growing environment, where the solutions with bounded relative error perform better. The anatomical constrains set the upper limit for the number of pyramidal cells in the medial entorhinal cortex around 200000 (Fig. 3.2 B, dashed line). Thus, the only solution, which is able to reach reasonable distances within the anatomical constrains is the grid solutions with bounded relative error (Table 3.1).

The different models are compared based on the total firing activity of the system, too (Fig. 3.3). During navigation, at each position, all the pre-DCs are activated which have one of their receptive fields at the actual position of the rat. The firing activity of the system can be calculated by counting the average number of cells that are simultaneously active at the same place. We found that in case of bounded absolute error the total activity of the system is proportional to the 2nd power of the largest scale (D_{max}), in all three models:

$$I^{ap}, I^{at}, I^{ag} \propto \mathcal{O}(D^2_{max}) \tag{3.4}$$

Similarly to the results on total cell numbers, the firing activity is largest in case of the place-pair model and smallest in case of the grid model (Appendix A.1, A.2).

When the relative error is bounded, the total cell activity in each position is propor-

tional to the logarithm of D_{max} in all three models:

$$I^{rp}, I^{rt}, I^{rg} \propto \mathcal{O}(\log(D_{max}), \tag{3.5}$$

and the grid model needs the less number of active cells (Appendix A.3, A.4). Since the action potentials consume the waste majority of energy in the brain, solutions with relative error bounds are much more economical, and the grid model produces the most effective result again.

Constraint	Absolute error			Relative error		
Model	place-pair	triangle	grid	place-pair	triangle	grid
Optimal scaling, S_i	linear			exponential		
Magnitude of the number of cells, $N(L)$	$\mathcal{O}(L^4)$			$\mathcal{O}(L^2)$		$\mathcal{O}(\log(L))$
Number of cells, N	$1.9 \cdot 10^9$	$6.3 \cdot 10^8$	$2.9 \cdot 10^8$	$5.6 \cdot 10^7$	$1.9 \cdot 10^7$	$1.5 \cdot 10^5$
Magnitude of the number of active cells , $I(D_{max})$	$\mathcal{O}(D_{max}^2)$			$\mathcal{O}(\log(D_{max})$		
Number of active cells, I	$1.1 \cdot 10^5$	$5.5 \cdot 10^4$	$1.8 \cdot 10^4$	$6 \cdot 10^3$	$3 \cdot 10^3$	$1 \cdot 10^3$

Table 3.1: **Summary of analytical results.** In order to compare the properties of different models, results are given for the three models in case of two different constraints on the error. The consecutive grid scales increases linearly in order to keep the absolute error of the distance estimation minimal, while increases exponentially for reaching optimal representation with bounded relative error. Magnitudes describe the scaling properties of cell numbers depending on the size of the environment. The concrete number of cells is calculated assuming an $L = 10\ m$ long environment in which the distance is measured from $S_1 = 30\ cm$ to $D_{max} = 5\ m$ maximal distance with $d = 3\ cm$ absolute or $C = 0.1$ relative error, assuming hexagonal discretization of the plane. In terms of both the required number of cells and the number of active cells, the grid model with bounded relative error achieves the most economical solution.

The analytical results above are summarized in Table 3.1. In case of both the bounded absolute and relative error, the grid model needs fewer neurons than the place-pair or triangle models. While the number of necessary neurons increases exponentially with the size of the environment in case of bounded absolute error and in place-pair and triangle models with bounded relative error, the rising rate of grid model with bounded relative error is only logarithmic. This rising rate is so slow, that it is likely to be close to the optimal solution. The previous models where the computational complexity (identified with the number of required cells) increases rapidly with the size of the environment, can work in a small environment but can not be extended to large territories. The average total firing activity of the neural system also increases logarithmically with the size of the largest spacing in case of bounded relative error and the grid model needs the least number of active cells in each position. We have shown that grid cells provide the possibility to build up a really scalable system, suitable to real world applications.

3.3 Distance coding based on the grid cell system

3.3.1 Model

The general model architecture is the following: grid cells innervate both DCs and feed-forward inhibitory neurons (FFINs) projecting to distance cells, and a competition among distance cells is executed by feed-back inhibitory cells (Fig. 3.4 A, B). Each distance cell and feed-forward inhibitory neuron is innervated by grid cells that share a common spacing, i.e. *has a scale* equaling this spatial periodicity and each inhibitory neuron projects to a distance cell that has the same scale. The two variants of this model only differ in the feed-forward connections from grid cells to the inhibitory neurons and DCs: in model A (Fig. 3.4 A) the effect of the feed-forward inhibitory cells on DCs is assumed to be negligible while model B (Fig. 3.4 B) assumes that distance cell activity is principally determined by the indirect effect through the inhibitory cells while direct excitation from the grid cells is not taken into account.

The grid cell firing pattern is similar to a triangular lattice so that grid cells fire at the vertices of the grid and are silent elsewhere (Fig. 3.4 C). Each grid cell can be characterized by three properties (Hafting et al., 2005): the spacing, orientation and a two dimensional phase of its grid. In the numerical simulations 110 spacings were randomly distributed in the [0.3-10] m interval following an exponential distribution and 1000 grid cells were simulated for each spacing value, resulting in a total number of 110000 grid cells. This number is in accordance with data about the number of cells in the upper layers of the entorhinal cortex (Andersen et al., 2007). For each grid cell, orientation and phase values were chosen randomly. To represent the grid cell activity in our model we applied the cosine grating model (Blair et al., 2007), which was used for computational efficiency and was not intended to represent an accurate biological model of grid cell firing activity. Thus, the location dependent firing rate of a given grid cell is calculated as

$$G^{S,\Theta,\mathbf{p}}(\mathbf{r}) = \xi(\mathbf{r}) \cdot \exp\left[0.3\left(\sum_{k=1}^{3}\cos(\boldsymbol{\omega}_k^{\Theta}\cdot(\frac{\mathbf{r}}{S}-\mathbf{p})) + \frac{3}{2}\right)\right] - 1, \qquad (3.6)$$

where S is the spacing, Θ is the orientation and $\mathbf{p} = (x_0, y_0)$ is the phase shift of the grid and $\mathbf{r} = (x, y)$ is the position of the rat in the arena. Cosine gratings were oriented according to the three vectors $\boldsymbol{\omega}_1^{\Theta}, \boldsymbol{\omega}_2^{\Theta}, \boldsymbol{\omega}_3^{\Theta}$ that had angles $\Theta - 30°$, $\Theta + 30°$

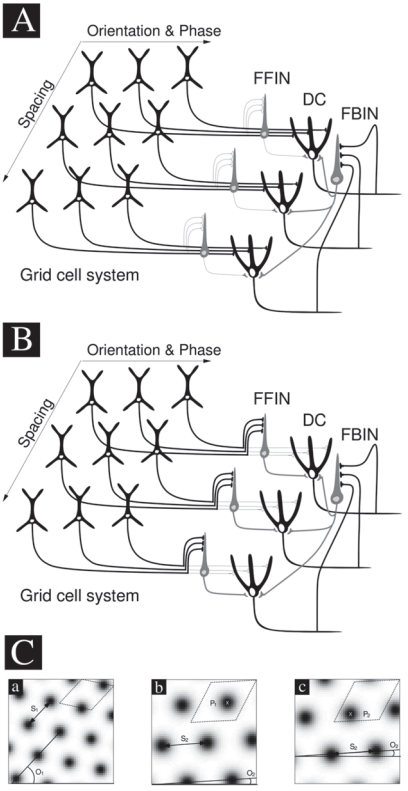

Figure 3.4: **Model architecture. A, B.** Entorhinal cortical pyramidal cells (the grid cell system) innervate distance cells (DC) and feed forward inhibitory neurons (FFIN). A given DC and FFIN receives synaptic contacts only from grid cells with a given spacing. In model A, direct input from grid cells to DCs is dominant and input from FFIN is negligible, while dominance of inputs is reversed in model B. A competition among DCs is realized by feedback interneurons (FBIN) resulting that only the DC receiving the largest net excitation remains active at each position. **C.** Examples of spatial activity patterns of grid cells. Firing frequency of three different grid cells in a rectangular arena are shown. Each grid cell is firing when the animal occupies the vertices of a triangular lattice (black spots) and is silent elsewhere (white areas). The exact firing pattern depends on the lattice that can be characterized by three properties: i) spacing (S_i) equals the distance between nearby firing fields, ii) orientation (O_i) falls in the range of 0-60 degrees and is defined by the angle between a horizontal line and the line on which nearby vertices are lying, iii) phase (P_i) is defined as the 2D location of the vertex falling in the 'basic unit' of the lattice (rhombus bordered by dotted line). Grid (a) is different from grid (b) and (c) in both spacing and orientation, while grid (b) and (c) differs from each other only in their phase. Note, that comparison of grid phases is reasonable only if the spacings and orientations of the grids are the same.

and $\Theta + 90°$, and an equal length of $4\pi/\sqrt{3}$. $\xi(\mathbf{r})$ is a random noise term taking values from a uniform distribution in the [1-1.15] interval realizing multiplicative noise of 7.5% on average. The sum of the three cosine functions ranged from $-3/2$ to 3, so the value of $\mathrm{G}(\mathbf{r})$ varied between 0 and $\sim$3.3. Note, that that the radius of a grid cell's subfields increase with the spacing of the grid cell.

Grid cells sharing a common spacing innervated the same postsynaptic cell (DC and feed-forward inhibitory neuron). The summed input from these grid cells is

$$D^S(\mathbf{r}) = \sum_{\Theta} \sum_{\mathbf{p}} G^{S,\Theta,\mathbf{p}}(\mathbf{r}) \mathbf{w}^{S,\Theta,\mathbf{p}}, \tag{3.7}$$

where $D^S(\mathbf{r})$ is the net input of the postsynaptic cell with scale S, $G^{S,\Theta,\mathbf{p}}(\mathbf{r})$ is the activity of a grid cell with spacing S, and $\mathbf{w}$ is the synaptic weight matrix.

Synaptic weights were assumed to be set by a one shot learning rule: when the animal occupies an emotionally significant place, i.e. *the origin*, synapses between grid cells having receptive field at the origin and postsynaptic cells innervated by them get long-term potentiated (Nakao et al., 2004; Abe et al., 2003), and synaptic weights become proportional to the firing frequency of the presynaptic grid cell in the origin (Blaise and Bronzino, 2003). This corresponds to Hebbian learning if firing activity of different DCs is assumed to be equal in the origin. According to these assumptions the synaptic weights stored the presynaptic firing rates at the important place:

$$\mathbf{w}^{S,\Theta,\mathbf{p}} = G^{S,\Theta,\mathbf{p}}(\mathbf{R}), \tag{3.8}$$

where $\mathbf{R}$ is the position of the origin. In our simulations, the origin was chosen to be the central point (coordinates: 0, 0) of a 20 x 20 m sized rectangular arena (Fig. 3.6, cross).

Feed-back inhibitory neurons realized a competition among distance cells so that only the DC receiving the highest net excitation was assumed to remain active in every spatial location.

Simulations were done in Matlab (version 7.3.0.298) on Linux operating system.

3.3.2 Results

The task that the model has to execute is to represent the distance of the animal from the origin by the population activity of distance cells. In model A, the activity of

a DC depends on the summed input received from its presynaptic grid cells, since effects from FFINs are assumed to be negligible. The constrain that a DC receives input from grid cells of a given spacing S results that the net input of the DC changes periodically with the distance from the origin, creating concentric rings around it (Fig. 3.6 A). A DC is exposed to large excitation, when the animal's distance from the origin is around an integer multiple of the scale of the DC (~$n \cdot S$) (Fig. 3.6 A, black rings). The alignment of the grid cell activity maxima deteriorates as the animal moves farther from the origin, which results in decreasing local maxima of the input to a given DC. At a given distance, the net input to the different DCs changes quasi-periodically as a function of the scale of the DCs (Fig. 3.5 A). Due to the competition among grid cells only the DC receiving the largest excitation remains active. Therefore, if there is an unambiguous correspondence between the distance and the scale of the active DC, the identity of the active distance cells would encode the distance of the animal from the origin. Figures 3.5 B and C demonstrates that in the distance range of effective coding (2.5-10.5 m, Fig. 3.5 B, dashed vertical lines), at most positions, the active DC's scale is around the distance to be estimated. However, in some cases, the largest input targets DC's of lower scales (Fig. 3.5 B, circled points), which makes the distance code ambiguous and decreases the estimation precision of the system. The standard deviation from the linear fitted in the effective coding range by least squares method is 84 cm. Note, that up to approximately 2.5 m distance the scale of the active DC equals the highest spacing of the grid system (10 m) which makes this system unable to estimate distances in this regime. The reason for this failure on short distances is that the diameter of one subfield of a grid cell increases with increasing spacing and the wider the receptive fields of a grid cell is, the less sensitive for small displacements from origin it is.

In model B, feed-forward excitation from grid cells to DCs are assumed to be negligible so DC activity is determined by the feed-forward inhibitory neurons. Again, the DC receiving the largest net input in any positions will be active, that is the one receiving the lowest inhibition from FFINs. Due to the learning rule, a FFIN receives small inputs at locations where the distance from origin is an integer multiple plus half of the DC's scale ($n \cdot S + S/2$) (Fig. 3.6 A, white rings). At a given position, the smallest excitation targets the inhibitory cell the scale of which approximately equals twice of the distance from origin (Fig. 3.5 A), therefore the active DC's scale is similarly twice of the distance to be estimated. This distance code is unambiguous in the 0.15-5.5 m distance regime (Fig. 3.5 B, C) and the standard

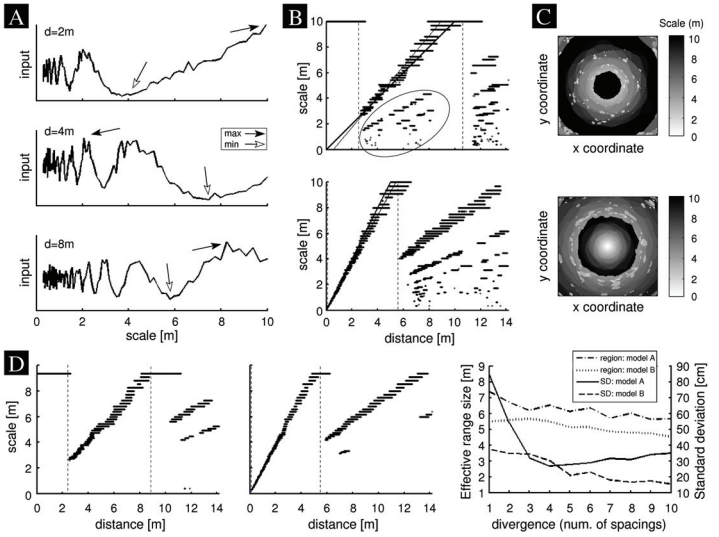

Figure 3.5: **Distance encoding. A.** Net input from grid cells to their postsynaptic cells (distance cells and feed-forward inhibitory neurons) with different scales at three different distances from the origin. At 2 m distance (upper graph) the highest input targets the cell with the largest scale (filled arrow), while the lowest input is received by cell with scale ~4 m that is approximately twice of the distance (empty arrow). This makes DCs of model B (but not model A) able to encode this distance. In case of 4 m distance (middle graph) model B is still working, since the lowest input is received by inhibitory neuron with scale around 8 m. The highest input is received by a cell the scale of which is smaller than the distance to be encoded, reflecting a false encoding in model A. However, note, that most of the distances in the ~2.5-10.5 m range are correctly encoded in model A. When distance from origin is 8 m (lower graph), model B is not able to encode the distance, while model A is working properly, the largest excitation is received by a DC that has a scale approximately equaling 8 m. **B.** The scale of the active DC as a function of the animal's distance from origin. In model A (upper graph) small distances can not be encoded by the DCs, since the DC with the largest scale is active at any distances in the 0-2.5 m range. In the 2.5-10.5 m range, the active DC's scale equals the distance to be estimated in most of the cases (points lying near the y=x linear i.e. the thick line), however there is a significant amount of positions where distance encoding is not correct (circled points). In model B (lower graph), distance encoding is correct up to ~5.5 m, i.e. approximately half of the largest scale. Points are dispersed near the y=2x linear (thick line) reflecting that each distance is represented by the DC with scale approximately equaling twice of the distance. In the range of effective coding (between vertical dashed lines) linear was fitted by the least squares method (thin lines). The standard deviation of the points in the above range from this line is significantly smaller for model B than for model A. **C.** Scale of the active DC in every positions of the rectangular arena for model A (upper subfigure) and model B (lower subfigure).

D. Distance estimation in case of divergence, i.e. when grid cells innervate more then one DCs and FFINs. Distance estimation is enhanced both for model A (left graph) and model B (middle graph) when each postsynaptic cell receives innervation from grid cells of five different but neighboring spacings: points in the range of effective coding (between vertical dashed lines) are less dispersed than in (B). With the increasing divergence (number of grid spacings innervating the same postsynaptic cell), the range of effective coding slowly decreases, however, the estimation error (standard deviation from the fitted linear in the effective range) is significantly decreasing both for model A and B (right graph).

deviation from the fitted linear is 38 cm.

In summary, (i) the smallest distance that can be estimated by model A is around one fourth of the highest grid spacing (2.5 m), while model B is able to encode distances as small as the half of the minimal spacing of the grid system (0.15 m), (ii) the upper bound of distance estimation ability equals about the largest spacing of the grid system in model A, while it is around the half of the maximal spacing in model B, (iii) in the distance ranges of effective coding (2.5-10.5 m for model A and 0.15-5.5 m for model B), model B has a significantly smaller estimation error than model A.

So far our model assumed a clearly convergent projection from grid cells to their postsynaptic cells: each grid cell innervated only one DC and FFIN while one postsynaptic cell received connections from several grid cells with the same spacing. In the followings we introduce divergence as well assuming that a grid cell innervates more than one DCs and FFINs so that a given cell receives innervation from all the grid cells with *similar* spacings. We tested the tolerance of the model, i.e. the size of effective coding range and the average error of the distance estimation, to the increasing number of neighboring grid spacings innervating one DC/FFIN. Figure 3.5 D shows that although the range of effective coding is slowly decreasing, the estimation precision is increasing with the increasing divergence. In case of model A, for a slight increase of divergence, the estimation error is significantly reduced, it becomes approximately one third of the error compared to the model assuming no divergence. This suggest that there is an optimal degree of divergence, which is large enough to significantly decrease the estimation error for both model A and B, but does not cause a remarkable decrease in the effective range size. In our simulation this was reached by the cases when each DC/FFIN received connections from grid cells with approximately five different (but neighboring) spacing values.

Figure 3.6 B and C show the firing pattern of DCs in model A and B (with no diver-

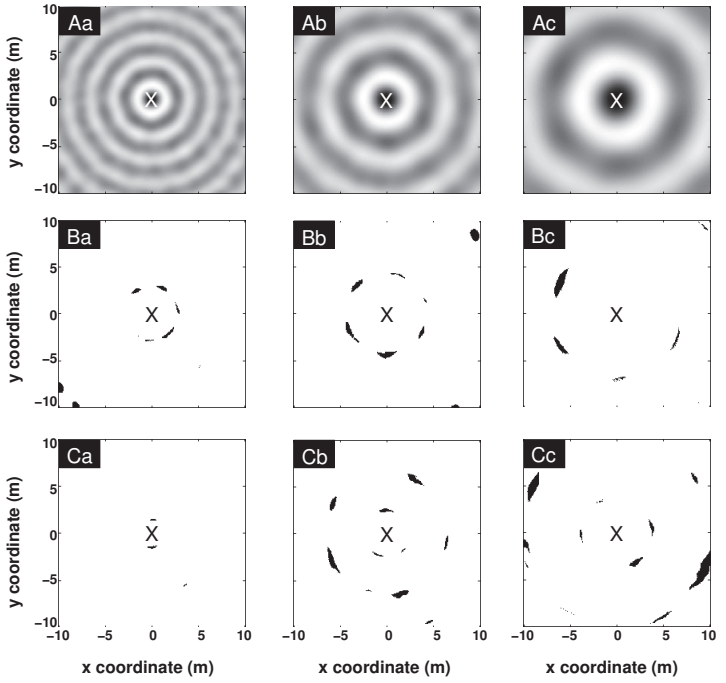

Figure 3.6: **Input and activity patterns. A.** Spatial input on the postsynaptic cells of the grid cell system. Net input of DCs in model A and FFINs in model B is organized into rings centered around the origin (cross). **B.** Activity pattern of DCs in model A. Introducing global feed-back inhibition between distance cells turns activity rings into patches organized on the ring with radius equaling the scale of the DC. **C.** Activity pattern of DCs in model B. Indirect input from grid cells through inhibitory neurons results that distance cells fire when the animal's distance from the origin equals half of the DC's scale (patches on the inner rings). Scales in the columns (a), (b) and (c) are ~2.9 m, ~4.6 m, and ~7.3 m, respectively.

gence), respectively. Due to the winner-take-all mechanism among DCs, concentric rings of net input on postsypatic cells of grid system (Fig. 3.6 A) were transformed into disjunct patches at a distance from origin approximately equaling the scale (model A) or half of the DC's scale (model B). These firing activity patterns are similar to the behavior of granule cells in the dentate gyrus region of the hippocampus (Jung and McNaughton, 1993; Leutgeb et al., 2007).

3.4 Discussion

In the short history of grid cells, most papers discuss their possible role in navigation in connection with hippocampal place representation. Up to now these articles attributed more or less the same role to the grid cell system: being involved in path integration it facilitates the creation of place cells in the hippocampus even in the absence of allothetic information (Burak et al., 2006; Fuhs and Touretzky, 2006; Franzius et al., 2006; Rolls and Kesner, 2006; Solstad et al., 2006). It is also often assumed, that grid cells perform path integration, thus change their firing rate according to the movement of the animal (Fuhs and Touretzky, 2006; Guanella et al., 2007; Burgess et al., 2007). In almost every model in the literature, firing pattern of grid cells is transformed to hippocampal place representation through competition among place cells receiving the summed activity of grid cells. However, the organization of the hippocampal place cell system is not topographic, therefore the metrical information, which is clearly present in the grid cell system, is lost in this way. For this reason, computational models dealing with the role of the hippocampal system in navigation of mammals, attributed a limited role to place cells, where learned connections between them store only the topology of the environment, but do not or minimally provide information on metrical relations (Foster et al., 2000; Trullier and Meyer, 2000). This topological representation is able to support a spatial navigation strategy, where a movement direction is associated to a given place during learning, however, this strategy can not account for many higher order navigation strategies, such as shortcut or detour finding in unknown areas. The ability of shortcut and detour finding is common among mammals and generally requires information about metric relations, distances and directions of the significant places in an environment (Trullier et al., 1997).

We propose that distance information, necessary to perform these navigation tasks, is extracted from the entorhinal cortical grid cell system and distance information is stored in the population firing activity of hypothesized distance cells that are innervated by grid cells. Analytical results suggests that the grid model implements an appropriate process for distance representation even in large environments. The sum of the estimated number of grid cells in EC layer II and pyramidal cells in layer III (which also show grid like activity (Sargolini et al., 2006)) is around 360000 (Andersen et al., 2007). Our calculations show that within these anatomical limits, the grid model is capable to measure distances up to real word distances, with at

most 10% relative error.

According to the architecture of our model, the hypothesized distance cells have to be located downstream of the entorhinal cortex. As grid cells in the EC layer II projects directly to the dentate gyrus of the hippocampus, we propose that distance cells can be most likely identified with the principal cells of dentate gyrus, the granule cells. Experimental findings support the view that the second stage of metric generation is related to dentate gyrus. Gilbert et al. (Gilbert et al., 1989) have developed a behavioral paradigm to study spatial pattern separation in rats: animals were trained to learn, which of two objects covered a baited food-well. The experiments revealed that lesions of the DG (but not the CA1) result in an inability of the animal to correctly separate spatially nearby locations (Gilbert et al., 2001), suggesting that the DG plays a specific role in distance determination. In another experiment (Goodrich-Hunsaker et al., 2008), dorsal DG lesioned rats have been shown to spend more time exploring the non-displaced objects than the metrically displaced objects, in contrast to control rats that behave conversely (Buhot et al., 1992); this indicates that the dorsal DG is required to generate a metric representation and mediate metric memory.

Our grid model relies on three main assumptions on the entorhino-hippocampal network:

First, it assumes, that grid cells with different spatial frequencies projects to different postsynaptic cell populations, i.e. granule cells and inhibitory interneurons of DG. This is in good agreement with the known anatomy of the perforant path projection, where the dorsolateral-to-ventromedial axis of the medial entorhinal cortex corresponds to the dorsal-to-ventral axis of the hippocampus (Fyhn et al., 2004). Furthermore, it is also known, that the dorsoventral gradient in the spatial scale of the grid fields (Hafting et al., 2005) is conserved in place field sizes of hippocampal place cells (Jung et al., 1994). However, the entorhinal cortex-gyrus dentatus projection is probably more dispersed than assumed by the basic model, in which each granule cell and inhibitory cell is innervated by grid cells that all have the same grid spacing (Dolorfo and Amaral, 1999). Therefore, we tested the behavior of the model assuming that a given DC and FFIN receives connections from grid cells of several similar spacings. We found that a slight increase in divergence significantly decreases the average estimation error of the model, thus, taking into account anatomically realistic projection distribution even approved the coding capabilities

of the system, although at the slight expense of the size of the distance range in which the estimation works (Fig. 3.5 D).

Second, each granule cell and interneuron is assumed to be innervated by grid cells with different orientations. In the pioneering paper of Hafting at al. (2005), grid cells recorded from the same tetrode were shown to share the same grid orientation. However, simultaneously recorded cells from non-corresponding locations in the left and right entorhinal cortices do sometimes have different grid orientations (Hafting et al., 2005), suggesting that more than one orientations are represented in one brain. In another experiment, measurements were made from several locations along the dorsoventral axis of dMEC in one hemisphere (Barry et al., 2007), and grid cells were found to have similar orientations (the largest difference in orientation between any two grids was 15 degrees, 25% of the maximally possible 60 degrees). However, grid orientation might show a gradient orthogonal to the dorsoventral axis (along which the spacing values increase), in which case differently oriented grids could be found along mediolateral or rostrocaudal axes. In conclusion, in order to decide whether our second assumption holds, the spatial distribution of grid orientations in the whole MEC has to be explored.

Third, we assume, that the grid cell synapses on the dentate granule cells and interneurons are potentiated in a one-shot manner when the animal occupies a significant place, and this potentiation is proportional to the presynaptic activity. This assumption is in accordance with the facts that the amygdala, which plays an important role in emotional arousal, can modulate synaptic plasticity at perforant path – DG synapses (Nakao et al., 2004) and that the strength of the long-term potentiation (LTP) indeed depends on the activation frequency (Blaise and Bronzino, 2003). A good candidate for the natural induction of LTP is the dentate EEG spike (Bramham, 1998) which is a large population activity occurring in the DG during awake immobility and slow wave sleep and is likely to be triggered by layer II cells of the entorhinal cortex (Bragin et al., 1995; Penttonen et al., 1997). Interestingly, these entorhinal neurons can generate population bursts (sharp potentials) during non-theta EEG pattern in cats which are abolished after amygdala lesion (Pare, 1995). The one-shot manner of our learning rule is in accordance with the theory that the hippocampus is responsible for episodic memory processes in higher mammals, as episodic memory requires fast, one-shot learning. In contrast to many navigational models that apply slow, incremental learning in order to form spatial representation (Káli and Dayan, 2000; Chavarriaga et al., 2005; Ujfalussy et al., 2008), our model

does not require a thorough exploration of the environment. The applied method of one-shot-learning and continuous comparison of the stored and actual patterns can be extended to other, non-spatial modalities as well.

These three assumptions, together with the known properties of the grid cell system, are enough to establish a system in the hippocampal dentate gyrus, which is able to continuously monitor the animal's distance from a selected, salient point. The mechanism of distance encoding is the following. The one-shot learning stores the momentary activity pattern of the grid cell system in the significant position at the synapse of grid cells on the dentate gyrus neurons. Thus, the output activity of these postsynaptic cells is proportional to the dot product of the stored and the actual activity pattern of the grid cell system, representing the similarity between the two. Considering the periodicity of the grid activity, this similarity became high whenever the animal moves an integer multiple of a grid period and low at the midpoints between them. When the animal is at a given distance from the origin, all the cells with divisor scales of the actual distance are receiving high input in this way. Since the highest among the divisors is the dividend itself, the activated distance cell with the highest scale represents the actual distance. According to experimental data (Hafting et al., 2005) the subfield diameter of a grid cell is increasing with increasing grid scale and this property is reflected in our model. As a result of this, the correlation between grid cells is increasing with the increasing scale, thus the heights of the peaks as well as the depths of the dips in the synaptic activation of dentate cells are increasing with the scale. Therefore, the most activated dentate cell has the highest scale while the scale of the least activated one is the double of it. Therefore, decoding the distance from this activity pattern can be achieved simply by selecting the dentate cell receiving either the largest (model A) or the smallest (model B) net excitation from the grid system. Identification of the activity minimum requires a transformation into activity maximum by local feed-forward inhibitory interneurons in model B. In this case, the firing pattern of these inhibitory cells in DG should also show spatial selectivity, which is in accordance with experimental findings (McNaughton et al., 1983; Kubie et al., 1990; Marshall et al., 2002). In both models, the distance cell receiving the largest net excitation can be chosen by competition among DCs realized by feedback inhibition, which leaves only the most activated cell active. This winner-take-all mechanism can be theoretically performed by the DG, where feed-back inhibition (Acsády and Káli, 2007) can realize a strong competition among granule cells.

The above mechanism resulted in a multi-peaked, patchy firing activity pattern of DCs, which is in general agreement with the experimental observation that a significant portion of DG granule cells have multiple place fields in an open environment (Jung and McNaughton, 1993; Leutgeb et al., 2007). However, these fields have not been reported to have a circular arrangement yet, as would be suggested by our model. This contradiction might be resolved in the following ways. (i) The circular firing property should be observable only in experiments, in which distance measuring from specific locations is important for the animal (which is not the case in most of the experiments). An optimal experiment would be for example in which the rat has to execute navigation task in a large open environment, containing a food source at a fixed position to where the animal has to find its way from many different positions. (ii) Instead of analyzing single cell activity, the geometrical analysis of the population activity of granule cells would be optimal to reveal the hidden regularity of the distance cell firing patterns. (iii) As our model required only a relatively small number of distance cells (in the presented simulations 110 distance cell for the estimation of distance from one location), it does not exclude the possibility that most of the dentate granule cells behave as place cells, and only a small portion are distance cells.

According to our model, information on distances from specific places arises in the dentate gyrus that projects to the CA region of the hippocampus. We hypothesize that distance cell activity might modulate the activity of CA3 place cells that encode the location of the animal, so that distance and position information would be associated. In this way, the distances of a position from the significant places of the environment become a subset of those important properties, which defines the identity of a position. Identity of a position can be defined by means of local properties, such as local view, smell and availability of food or water etc. and by means of more global properties, such as distances or directions of important objects. All of these properties can serve the identification of a place, but can drive the animals too. In an advanced navigational system, the animal should be able to search for an actual aim based not only on its elementary needs such as hunger or thirst but also based on environmental topology or metrics. Topological search makes possible to find those places that are available from a given location or from where the given location is available while metrical search helps to find those places that are close to or in a given distance from the referential points of the environment. Feed-forward association of these distances to positions makes possible this metrical search. An

experimental finding supporting this view is that place cells can show goal dependent activity (Ainge et al., 2007).

In the present chapter we introduced a model which is able to keep track of the animal's distance from one specific point. However, the proposed method could be extended easily to represent distances from more than one significant places or objects, by introducing parallel distance cell systems competing during learning. It is important to note that the number of grid cells does not have to be increased in order to represent distances from several origins. Only the number of required distance cells increases with the number of significant places, however the proposed model needs so small amount of DCs compared to the number of DG granule cells, that a vast number of DC systems (representing distances from different locations) can exist in the DG. We hypothesize that the several DC systems would be able to support many navigational systems and strategies such as self-localization and route planning.

4

Conclusions

In the present dissertation we studied the activity of place cells that encode the location of rodents during navigation and set up a model that achieves the determination of distances from places that the animal has previously visited.

Regarding place cell activity, dendritic long term integration of inputs and the mechanism of rate and phase code generation was studied in detail. By numerical simulations of a conductance-based two-compartmental hippocampal pyramidal cell model we showed that:

- Periodic dendritic spiking integrates inputs by shifting the phase relative to an external oscillation and this generates the phase code. The number of somatic action potentials triggered by the dendritic spike depends on the instantaneous level of somatic depolarization, which results in rate coded firing of place cells. This mechanism resulted in firing patterns that closely matched experimental data from hippocampal place cells of freely behaving rats.

- After the cessation of increased input in the place field, free-running phase shift drives dendritic spiking back to the stable baseline firing at which dendritic spikes they can not evoke somatic firing. This free-running phase shift is independent from the running speed of the animal therefore correlation between firing phase and position of the animal is smaller in the second half of the place field than in the first half.

- Somatic input is proportional to the running speed of the animal and modulates the firing rate of the cell while leaving firing phases relatively unaffected. Therefore, faster runs through the same place field are associated with higher firing rates while the firing phase–position relationship do not show any systematic changes. This results in a specific decoupling of the rate and phase code of place cells.

We showed that the time-constant of the dendritic integration process is practically infinite for input intensities above a threshold and can be still several hundred milliseconds long below this threshold. Due to the free-running phase shift of dendritic spikes the cell can show firing activity for several hundred milliseconds after the stimulation. This is a potential single cell mechanism for the generation of persistent activity that is a long-lasting change in neural firing rates after transient stimulation. Similar mechanisms might account for the firing pattern of cells outside the hippocampus during working memory tasks.

For studying distance representation, three models were set up: the first two models executed distance estimation without the grid cell system while in the third model distance information is extracted from the activity of grid cells. We found that:

- The grid model needs remarkably less neurons than the two other models functioning without grid cells. While the number of necessary neurons in these models increases exponentially with the size of the environment the rising rate in the grid model is logarithmic. Similarly, the number of active neurons in a certain position is the lowest in case of the grid model. Thus, the system using grid cells realizes the most effective distance coding in terms of both cell numbers and average firing activity.

- Storing the momentary activity pattern of the grid cell system in a freely chosen position by one-shot learning and comparing it to the actual grid activity at other positions results in a distance dependent activity of distance cells. The distance between the two places is represented by the active distance cell at the actual position of the animal.

- By direct decoding (model A) the largest representable distance equals to the largest grid spacing but the system fails to encode smaller distances (up to the quarter of the maximal spacing). By indirect decoding (model B) the system provides precise distance determination up to the half of the largest grid spacing.

- The precision of distance representation depends on the divergence of the connectivity between grid cells and distance cells: distance estimation is more precise if the same postsynaptic cell is innervated by grid cells of different similar spacings.

- The simulated distance cells have a multi-peaked, patchy spatial activity pattern where the distances of receptive fields from the significant position are equal.

Analytical results suggests that the grid model implements an appropriate process for distance representation even in large environments. The analytical calculations show that, within the known anatomical limits on the cell numbers, the grid model is capable to realize distance estimation in a large distance range (0-10 m) by which real-world navigation tasks can be performed. According to the architecture of the suggested model, the hypothesized distance cells have to be located down-stream of the entorhinal cortex. As grid cells in the entorhinal cortex projects directly to the dentate gyrus of the hippocampus, we propose that distance cells can be identified with the granule cells of dentate gyrus. This is further supported by the simulation results showing that distance cells have an activity pattern consistent with the experimentally observed behavior of granule cells.

A

Appendix

A.1 Calculation of cell numbers in the place-pair and the triangle models with bounded absolute error

Let us denote the linear extension of the environment by L. The area of the environment is proportional to L^2 and this area should be discretized into distinct places in order to represent it with finite number of cells. Considering only regular tessellations, three types of lattices can be used for discretization: triangular, square and hexagonal lattices (Fig. A.1 B). Note, that triangular and hexagonal lattices are complementer to each other (the centers of units in a hexagonal grid forms a triangular lattice and vice-versa) while square lattice is its own complementer. The discrete representation of the continuous space naturally leads to representational error, since each unit of the lattice is represented only by its center. In order to keep the *absolute error* of distance determination under d, no point of a discretization unit should be farther than $d/2$ from the center of the unit (Fig. A.1 A). With this constrain the maximal area of the discretization units is $T = Ad^2$, where the A should be substituted with $A^t = 3\sqrt{3}/16 \approx 0.325$ for triangular, $A^s = 1/2$ for square and $A^h = 3\sqrt{3}/8 \approx 0.65$ for hexagonal units. This shows, that the area of the hexagonal unit is the largest among the three possible units. Thus, the most economical way of discretization is using hexagonal lattice. Assuming economical representation, the receptive fields of the neurons representing the hexagonal units should form a triangular grid.

Based on this discretization, a pre-distance cell system can be defined by connecting each pair of discretization units with a given distance to a pre-distance cell. The behavior of such a pre-distance cell system in one dimension is shown on Fig. A.2 A. In one dimension, any point pair can be described by the position of the first point (phase) and the distance between the two points. The length of the smallest diagonal

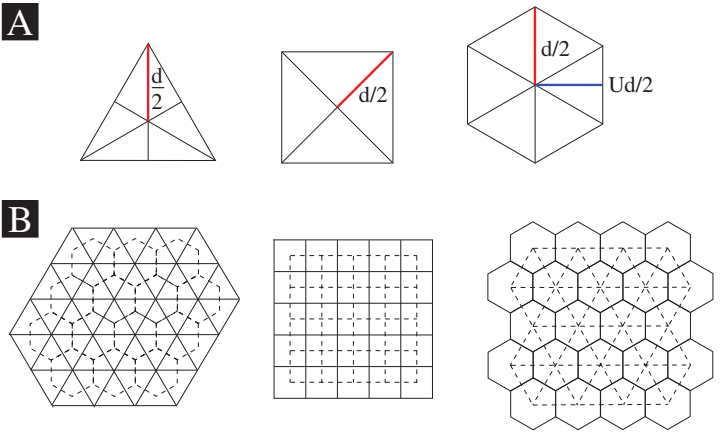

Figure A.1: **Discretization of the plane. A.** The three possible discretization units, under the constrain, that no points of a unit should be farther than $d/2$ from the center. **B.** The triangular, square and hexagonal discretization lattices. Complementer lattices formed by the center points are shown with dashed lines.

of the d diameter hexagon is Ud, where $U = \sqrt{3}/2$. Thus we will represent the hexagonal units of the discretization in one dimension with intervals of length Ud, marked with gray triangles in Fig. A.2 A. This description of position pairs by the points of the phase-distance plane allows the determination of which set of position pairs activates which pre-distance cell. This set of points, are called "the field of responsibility" here, and can be considered as a receptive field of a pre-distance cell in the abstract space of the position pairs. Each gray parallelogram on Fig. A.2 A shows the field of responsibility of a pre-distance cell. Using this chart, the distribution of scales e.g. the discretization of the output distance could be derived from the requirement, that the distance between any two points of the plane should be represented by an absolute error less than a given d constant. In order to fulfill this requirement, the width of the each receptive field should not be longer than Ud and this results in parallelogram shaped fields of responsibility plotted on Fig. A.2 A, of which horizontal projection and vertical sidelengths are equal to Ud. This shows that the distance, to which a cell responds, depends on the phase, but no point of these parallelograms is farther than Ud from the scale level S_i, thus each parallelogram fulfills the above requirement. After this, the task is to tessellate the phase-distance plane by these parallelograms without gaps. The chains of light and

dark gray parallelograms marks the fields of responsibility of the two cell population corresponding to the first two scales S_1 and S_2 on Fig. A.2 A. These two sawtooth patterns can be fitted to each other only if

$$S_{i+1} - S_i = Ud \tag{A.1}$$

and the two populations of the cells use the same receptive field system. If the receptive field systems of the two populations are relatively shifted to each other, the gaps between the two sawtooth patterns can not be avoided. In this case, overlapping receptive fields are required (Fig. A.2 B). Doubling the number of these one dimensional pre-distance cells and using overlapping receptive fields ensure that every point on the phase-distance plane, thus every position pair between $S_i - \frac{Ud}{2}$ and $S_i + \frac{Ud}{2}$ distance is covered by at least one field of responsibility. Two consecutive scales can be fitted to each other again, if $S_{i+1} - S_i = Ud$. There are overlaps also in the phase-distance plane (darkest small gray parallelograms in Fig. A.2 B), thus there are position pairs to which more than one cell responds. They are coding the same or similar distances (neighboring scales) and both scales give the real distances with error less than Ud, thus the original requirement is fulfilled.

In two dimensions, three shifted, but overlapping cell populations are enough to ensure the existence of a finite length distance regime to which cells of a population respond regardless of the two dimensional phase of the position pairs (Fig. A.2 C). Thus, depending on the implementation, if the same discretization can not be used in all scales, three times more cells should be used in one scale.

From Eq. A.1 it can be concluded, that in case of bounded absolute error, scales should be distributed linearly, with steps Ud, thus:

$$S_i = i \cdot U \cdot d. \tag{A.2}$$

If the longest scale is denoted by D_{max}, the number of required scales can be determined as:

$$\sigma^a(D_{max}) = \frac{D_{max}}{Ud}. \tag{A.3}$$

The place-pair model of distance determination assigns one pre-distance cell to each pair of places (Fig. 3.1 A), thus the number of required pre-distance cells can be calculated by counting the number of possible place pairs.

In order to simplify the calculations a triangular environment will be assumed with side length L. This environment is discretized into hexagons with diameter d, which

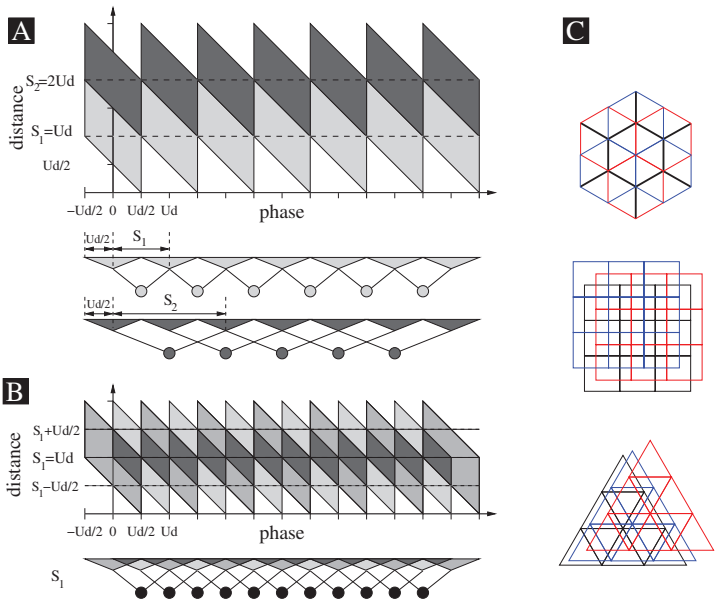

Figure A.2: **Tesselation of the phase-distance plane in one-dimensional case. A.** In this example, two populations of distance cells (light and darker gray circles), corresponding to the first and second scale (S_1 and S_2) illustrate the behavior of distance cell system in bounded absolute error case with fixed receptive fields. Gray triangles correspond to the one-dimensional receptive fields with Ud diameter. Light gray parallelograms mark the distances on which the cells of the first scale react, depending on the position (phase) of the first point being addressed. Similarly, dark gray area shows the field of responsibility for the cells of second scales. The light and dark sawteeth fit into each other without gap only if $S_2 - S_1 = Ud$ and the two distance cell populations use the same receptive field system. If the two receptive field systems are relatively shifted, gaps between the two fields of responsibility can not be avoided. **B.** If different scales use different receptive fields, overlapping receptive fields are required in each scale to ensure that at least one distance cell responds to distances between $S_i - Ud/2$ and $S_i + Ud/2$ in all phases. **C.** Examples of overlapping receptive fields in two dimensional cases. In all three grids, three cell populations of which receptive fields are marked with black, red and blue are able to ensure the existence of a distance regime to which these distance cells respond (similarly to subfigure B).

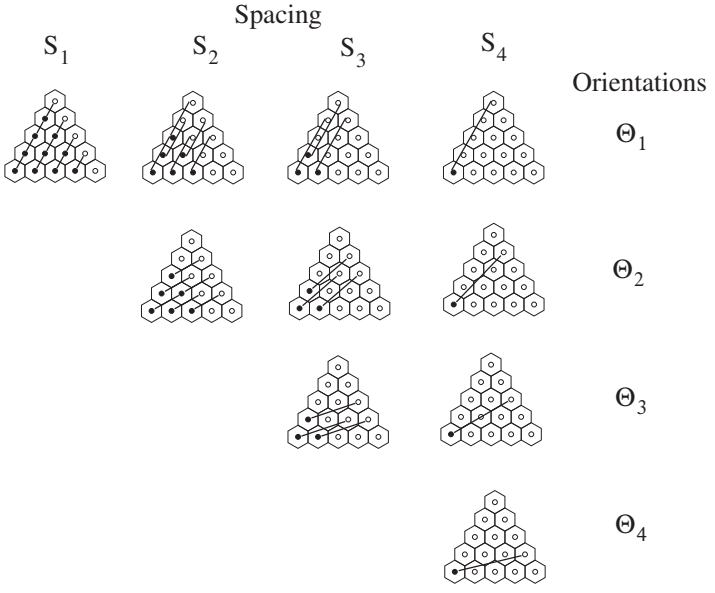

Figure A.3: **Decomposition of the connections according to distances and orientations.** A triangular environment is discretized into hexagonal patches. The connections between them is decomposed according to the scales S_i and orientations Θ_j. The number of possible orientations increases with the scales. Black dots show the possible shifts, each black dot corresponds to one end of a connection. The number of possible shifts decreases with the scales and is independent from the orientation. Similar connections are possible in two other directions, according to the 60° rotational symmetry of the grid, which are not shown here. Thus, in order to count all the connections, 3 times more shifts should be considered and should be summed up for all orientations and scales.

results a triangular grid for the centers of the hexagonal discretization units with periodicity Ud, where $U = \sqrt{3}/2$. The coordination number of this grid equals the number of nearest neighbors in the grid that is $Q = 6$. Figure A.3 shows that the number of connections (N_{ij}^{ap}) on scale S_i in a particular orientation Θ_j is given by the number of hexagons in a triangle with side length $L - S_i$:

$$N_{ij}^{ap} = \frac{Q}{2} \sum_{k=1}^{\frac{L-S_i}{Ud}+1} k = \frac{Q}{4} \left(\frac{L-S_i}{Ud} + 1 \right) \left(\frac{L-S_i}{Ud} + 2 \right) \approx \frac{Q}{4} \left(\frac{L-S_i}{Ud} \right)^2 . \tag{A.4}$$

In case of a triangular environment, the number of connections N_{ij}^{ap} is independent of the orientation (Fig. A.3).

For the rotations note, that in case of a triangular lattice after 60° rotation the original lattice is reached. Thus, in order to cover the circle with radius S_i by the d diameter patches,

$$O_i^a = \frac{S_i}{Ud} = i \tag{A.5}$$

rotations are required.

Substituting $S_i = iUd$ into Eq. A.4 and summing up for all orientations according to Eq. A.5 the number of connections on one scale is:

$$N_i^{ap} = \sum_{j=1}^{i} N_{ij}^{ap} \approx \frac{Q}{4} \left(i \frac{L^2}{U^2 d^2} - i^2 \frac{2L}{Ud} + i^3 \right) . \tag{A.6}$$

The total number of connections (N^{ap}) up to the maximal length D_{max} is given by:

$$N^{ap} = \sum_{i=1}^{\sigma^a(D_{max})} N_i^{ap} \approx \frac{Q}{4} \sum_{i=1}^{\frac{D_{max}}{Ud}} \left(i \frac{L^2}{U^2 d^2} - i^2 \frac{2L}{Ud} + i^3 \right) . \tag{A.7}$$

Performing the summation, all the three terms contribute to the leading order:

$$N^{ap} = \frac{Q}{4} \frac{D_{max}^2}{U^4 d^4} \left(\frac{L^2}{2} - \frac{2LD_{max}}{3} + \frac{D_{max}^2}{4} \right) . \tag{A.8}$$

Considering the case where $D_{max} = \frac{L}{2}$ as an example and substituting $U = \frac{\sqrt{3}}{2}$ and $Q = 6$ results in:

$$N^{ap} = \frac{33}{384} \frac{L^4}{U^4 d^4} \approx \frac{11}{72} \frac{L^4}{d^4} \approx 0.15 \frac{L^4}{d^4} . \tag{A.9}$$

In order to count the necessary pre-distance cells for the triangle model, places in the vertices of an equilateral triangle are represented by the same pre-distance cell.

Since one triangle corresponds to three connections, the number of necessary pre-distance cells decreases by the a factor 3. Thus similar to the Eq. A.8, the triangle model requires

$$N^{at} = \frac{Q}{12}\frac{D_{max}^2}{U^4 d^4}\left(\frac{L^2}{2} - \frac{2LD_{max}}{3} + \frac{D_{max}^2}{4}\right) \tag{A.10}$$

pre-distance cells.

In the same particular case, when $D_{max} = \frac{L}{2}$, this results in

$$N^{at} = \frac{11}{384}\frac{L^4}{U^4 d^4} \approx \frac{11}{216}\frac{L^4}{d^4} \approx 0.05\frac{L^4}{d^4}. \tag{A.11}$$

However, typically not all places can be organized into triangles, thus Eqs. A.10 and A.11 underestimates the necessary number of pre-DCs.

The total firing activity of the system is proportional to the average number of cells that are active at the same time. While the rat is wondering around his environment, in each position, pre-distance cells which have one of their receptive fields in the actual location of the rat are activated. The actual position of the rat appoints one phase among the possible connections (Fig. A.4 A). Thus, the total activity of the place-pair cell system can be found by summing up all connections in all scales in all directions but in one phase:

$$I^{ap} = \sum_{i=1}^{\frac{D_{max}}{Ud}} \sum_{j=1}^{i} Q \approx \frac{Q}{2}\frac{D_{max}^2}{U^2 d^2} = 3\frac{D_{max}^2}{U^2 d^2}. \tag{A.12}$$

In the triangle model, the rat activates $\frac{Q}{2}$ triangles in one location, one scale and one direction (Fig. A.4 B). Thus the activity of the triangle model network is given by:

$$I^{at} = \sum_{i=1}^{\frac{D_{max}}{Ud}} \sum_{j=1}^{i} \frac{Q}{2} \approx \frac{Q}{4}\frac{D_{max}^2}{U^2 d^2} = \frac{3}{2}\frac{D_{max}^2}{U^2 d^2}. \tag{A.13}$$

A.2 Calculation of cell numbers in the grid model with bounded absolute error

To calculate the number of necessary grid cells, a new description is introduced. After discretization of the plane, all possible connections are decomposed into regular triangular grids, according to three parameters: the periodicity of the grids i.e.

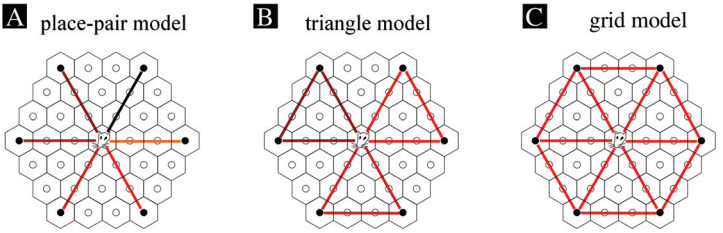

Figure A.4: **The activated connections by the actual position of the rat. A.** The actual position of the rat (in the center) activates 6 pre-DCs in the place-pair model in one scale and one orientation, which corresponds to the Q coordination number of the triangular grid formed by the center points. **B.** In the triangle model, the rat activates 3 pre-DCs in one scale and one orientation, corresponding to the 3 triangles. **C.** In the grid model, only 1 lattice is activated among all the phase shifts in one scale and one orientation.

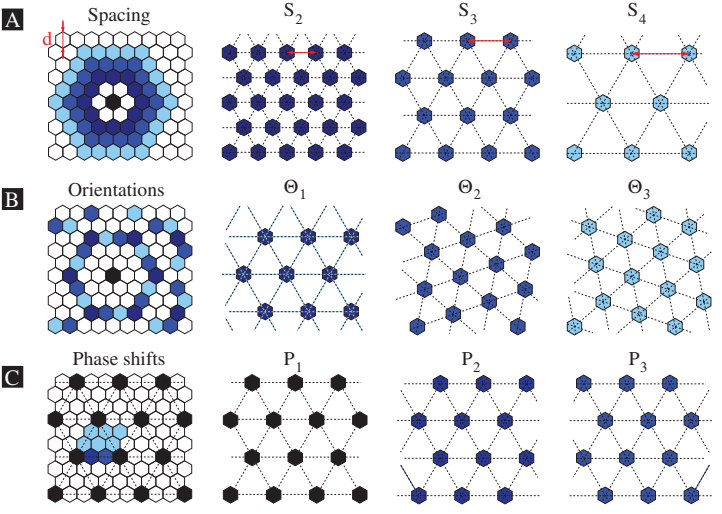

Figure A.5: **Decomposition of all connections into edges of regular grids. A.** Distance is decomposed into scales S_i marked with different colors, resulting grids with different spacings. **B.** discretization of directions resulted in grids with different orientations Θ_j. **C.** Description of all connections in one scale in one direction requires phase shifted lattices P_i to cover the whole plane. While the black patch wanders over the area of the colored patches, forming the rhomboid basic unit of the grid, the patches of the shifted lattices cover the whole plane.

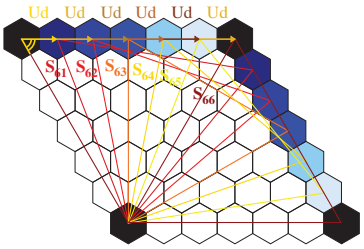

Figure A.6: **Changes of the grid periodicity by the orientation.** There are i possible orientations, indexed by j, on the i^{th} scale. The changes of the S_{ij} periodicity are described by the law of cosine, applied to the 60 ° arch labeled by double line. The periodicity decreases with j until the $j \leq i/2$ and increases above.

scales which correspond to the represented distances, the orientations of the grids and the two dimensional phase shifts (Fig. A.5).

The periodicity of the lattice depends not only on the scale, but also on the orientation of the lattice. (Fig. A.6.) The effect of rotation can be expressed by the law of cosines. The S_{ij} periodicity on the i^{th} scale and j^{th} orientation is:

$$S_{ij}^2 = S_i^2 + (jUd)^2 - 2S_i jUd * cos\left(\frac{\pi}{3}\right). \tag{A.14}$$

There are i possible orientations for a grid with periodicity S_i and the rotation decreases the S_{ij} until $j < i/2$ and increases after.

In order to cover all place pairs on the plane with regular triangular grids, each grid with a given scale and orientation should be shifted into every directions until the shift-symmetry of the lattice is reached and the lattice becomes identical to the original one. While doing so, each d diameter hexagonal patch around the vertex of the grid wanders between the neighboring vertices. The covered area could be called basic cell or unit cell of the lattice, but as the cell notation can cause confusions in the context of neuroscience, we will use the basic unit term. In a triangular lattice with periodicity S_{ij}, the basic unit can be chosen as a rhombus with sidelength S_{ij} (Fig. A.5 C). To cover the whole plane, with the hexagonal patches in the vertices of the lattice, only one basic unit should be covered with one patch. The extension of a patch in the directions of the basic unit sides is Ud, thus the number of necessary phase shifts of patches is:

$$P_{ij} = \frac{S_{ij}^2}{U^2 d^2}. \tag{A.15}$$

Substituting S_{ij} from Eq. A.14 results in:

$$P_{ij} = i^2 - ij + j^2. \tag{A.16}$$

The number of cells required for one scale is the sum of all phases for all orientations:

$$N_i^{ag} = \sum_{j=1}^{O^a} P_{ij} = \sum_{j=1}^{i} \left(i^2 - ij + j^2\right) \approx \frac{5}{6} i^3. \tag{A.17}$$

Thus the total number of necessary grid cells is expressed as:

$$N^{ag} = \sum_{i=1}^{\frac{D_{max}}{Ud}} N_i^{ag}, \tag{A.18}$$

where i goes through all the scales. Performing the summation and keeping the leading order only:

$$N^{ag} = \sum_{i=1}^{\frac{D_{max}}{Ud}} \frac{5}{6} i^3 \approx \frac{5}{24} \frac{D_{max}^4}{U^4 d^4}. \tag{A.19}$$

Assuming $D_{max} = \frac{L}{2}$ and substituting $U = \frac{\sqrt{3}}{2}$ led to:

$$N^{ag} = \frac{5}{216} \frac{L^4}{d^4} \approx 0.023 \frac{L^4}{d^4}. \tag{A.20}$$

The location of the rat unambiguously determines the phase of the activated grid in one scale and one orientation. Thus, there is only one phase of grids in each orientation and scale which can be activated at the same time (Fig. A.4 C), so the activity of the network i.e. the number of simultaneously active cells can be calculated as:

$$I^{ag} = \sum_{i=1}^{\frac{D_{max}}{Ud}} \sum_{j=1}^{i} 1 \approx \frac{1}{2} \frac{D_{max}^2}{U^2 d^2}. \tag{A.21}$$

Summations can be performed using the following forms:

$$\begin{aligned} &\textstyle\sum_{i=1}^{N} i = \frac{(N+1)^2}{2} \approx \frac{N^2}{2} \\ &\textstyle\sum_{i=1}^{N} i^2 = \frac{N(N+1)(2N+1)}{6} \approx \frac{N^3}{3} \\ &\textstyle\sum_{i=1}^{N} i^3 = \frac{N^2(N+1)^2}{4} \approx \frac{N^4}{4} \end{aligned} \tag{A.22}$$

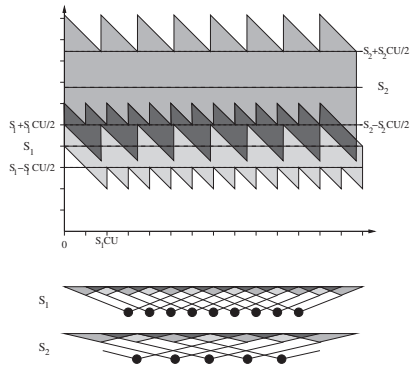

Figure A.7: **Tessellation of the phase-distance plane in one-dimensional case for bounded relative error.** Fields of responsibility for the first two scales of distance cells are marked with lighter and darker gray sawtooth stripes. In case of relative error, the receptive fields differ on different scales, thus each scale should consist of two overlapping populations. The darkest gray marks the overlaps between fields of responsibility of these neighboring scales. In this overlapping area the cells of both scales are respond and give the real distances within the relative error limit C.

A.3 Calculation of cell numbers in the place-pair and the triangle models with bounded relative error

The number of neurons required in the above solutions scales as $\left(\frac{L}{d}\right)^4$, which results in a huge number of neurons in a large environment. However, the strict requirement for the bounded absolute error can be weakened. Typically, for larger distances higher error could be allowed, which means that only the *relative error* is required to be smaller than a given C constant:

$$\frac{d_i}{US_i} \leq C, \tag{A.23}$$

where US_i is the smallest distance on the i^{th} scale. While in case of bounded absolute error, the same d error was allowed in all scales, here the maximal allowed error d_i increases with the increasing scales:

$$d_i = C \cdot U \cdot S_i. \tag{A.24}$$

Figure A.7 shows the behavior of a one dimensional distance cell system of two scales with bounded relative error. From the basic requirement of Eq. A.23 the

necessary number of scales and their optimal distribution can be determined:

$$S_i + \frac{S_i CU}{2} = S_{i+1} - \frac{S_{i+1} CU}{2}. \tag{A.25}$$

From this:

$$S_{i+1} = S_i \cdot \frac{2 + CU}{2 - CU} \tag{A.26}$$

and

$$S_i = S_1 \left(\frac{2 + CU}{2 - CU} \right)^{i-1}, \tag{A.27}$$

where S_1 is the smallest scale to be measured. Thus, scales should be distributed exponentially, in other words scales should form a geometrical series with quotient

$$q = \frac{2 + CU}{2 - CU}. \tag{A.28}$$

The largest distance to be measured is D_{max}, thus:

$$D_{max} = S_1 \left(\frac{2 + CU}{2 - CU} \right)^{\sigma^r(D_{max})-1}, \tag{A.29}$$

where the number of the required scales is the smallest integer which is greater than $\sigma^r(D_{max})$. From this, the number of necessary scales is:

$$\sigma^r(D_{max}) = \log_{\frac{2+CU}{2-CU}} \frac{D_{max}}{S_1} + 1 = \frac{\log \frac{D_{max}}{S_1}}{\log \frac{2+CU}{2-CU}} + 1. \tag{A.30}$$

After determination of the distance scales, a similar scene as in the case of bounded absolute error is used. In Appendix A.1 the total connections in each scale are decomposed according to different orientations and shifts. In this section the fixed d absolute error is changed to a scale dependent d_i error according to Eq. A.24. Similarly to Eq. A.4:

$$N_{ij}^{rp} \approx \frac{3Q}{4} \left(\frac{L - S_i}{U d_i} \right)^2. \tag{A.31}$$

Increasing size of discretization units in case of bounded relative error requires different discretization grids for every scales, thus 3 times more phase shifted cell should be used for every scales (Fig. A.2 and A.7).

Substituting d_i according to Eq. A.24 and S_i from Eq. A.27 and using the q notations according to Eq. A.28 results in:

$$N_{ij}^{rp} \approx \frac{3Q}{4U^4C^2} \left(\frac{L^2}{S_1^2} \frac{1}{q^{2(i-1)}} - \frac{L}{S_1} \frac{2}{q^{i-1}} + 1 \right). \tag{A.32}$$

The number of necessary orientations is:

$$O_i^r = \frac{S_i}{Ud_i} = \frac{1}{C}. \tag{A.33}$$

The number of connections in one scale is calculated as a sum of N_{ij}^{rp} for all possible orientations:

$$N_i^{rp} = \sum_{j=1}^{O_i^r} N_{ij}^{rp} \approx \frac{3Q}{4U^4C^2} \sum_{j=1}^{1/C} \left(\frac{L^2}{S_1^2} \frac{1}{q^{2(i-1)}} - \frac{L}{S_1} \frac{2}{q^{i-1}} + 1 \right) =$$

$$= \frac{3Q}{4U^4C^3} \left(\frac{L^2}{S_1^2} \frac{1}{q^{2(i-1)}} - \frac{L}{S_1} \frac{2}{q^{i-1}} + 1 \right). \tag{A.34}$$

Keeping only the leading order led to:

$$N_i^{rp} \approx \frac{3Q}{4U^4C^3} \frac{L^2}{S_1^2} \frac{1}{q^{2(i-1)}}. \tag{A.35}$$

The total number of connections, thus the number of necessary pre-DCs in the place-pair model is calculated by summing up N_i^{rp} for all scales:

$$N^{rp} = \sum_{i=1}^{\sigma^r(D_{max})} N_i^{rp} \approx \frac{3Q}{4U^4C^3} \frac{L^2}{S_1^2} \sum_{i=1}^{\sigma^r(D_{max})} \frac{1}{q^{2(i-1)}}. \tag{A.36}$$

Assuming, that $\sigma(D_{max})$ is high enough, this results in:

$$N^{rp} \approx \frac{3Q}{4U^4C^3} \frac{L^2}{S_1^2} \frac{q^2}{q^2-1} = 8 \frac{1}{C^3} \frac{L^2}{S_1^2} \frac{q^2}{q^2-1}, \tag{A.37}$$

where the summation was performed by using the form for sum of geometrical series:

$$\sum_{i=1}^{\infty} q^{i-1} = \frac{1}{1-q}. \tag{A.38}$$

In the triangle model, a factor of 3 is gained by representing places in the vertices of an equilateral triangle by the same distance cell, resulting in:

$$N^{rt} \approx \frac{Q}{4U^4C^3} \frac{L^2}{S_1^2} \frac{q^2}{q^2-1} \approx \frac{8}{3} \frac{1}{C^3} \frac{L^2}{S_1^2} \frac{q^2}{q^2-1}. \tag{A.39}$$

The three overlapping population of cells should be considered during calculation of the total network activity. Similar to the Eq. A.12:

$$I^{rp} = \sum_{i=1}^{\sigma^r(D_{max})} \sum_{j=1}^{1/C} 3Q = \frac{3Q}{C} \sigma(D_{max}) = \frac{18}{C} \left(\frac{\log \frac{D_{max}}{S_1}}{\log \frac{2+CU}{2-CU}} + 1 \right). \tag{A.40}$$

Parallel to the Eq. A.13 the activity in the triangle model is decreased by a factor 2 compared to the place-pair network:

$$I^{rt} = \sum_{i=1}^{\sigma^r(D_{max})} \sum_{j=1}^{1/C} \frac{3Q}{2} = \frac{3Q}{2C}\sigma(D_{max}) = \frac{9}{C}\left(\frac{\log \frac{D_{max}}{S_1}}{\log \frac{2+CU}{2-CU}} + 1\right). \tag{A.41}$$

A.4 Calculation of cell numbers in the grid model with bounded relative error

In order to get the number of necessary grid cells in case of bounded relative error, the similar description is used as in Appendix A.2. The total connections are discretized into triangular grids with different distance scales, orientations and phases. Keeping the relative error bounded, geometrical discretization of scales according to Eq. A.27 and the discretization of orientations according to Eq. A.33 are required. The number of required shifted grids on one scale and orientation is expressed similarly to the Eq. A.15, but by changing the scale independent d into the scale dependent d_i:

$$P_{ij}^{rg} = \frac{S_{ij}^2}{U^2 d_i^2} \tag{A.42}$$

Substituting S_{ij} from Eq. A.14 leads to:

$$P_{ij}^{rg} = \frac{S_i^2 + U^2 j^2 d_i^2 - S_i U j d_i}{U^2 d_i^2} = \frac{S_i^2}{U^2 d_i^2} + j^2 - \frac{j S_i}{U d_i}. \tag{A.43}$$

Substituting d_i from Eq. A.24 leads to:

$$P_{ij}^{rg} = \frac{1}{U^4 C^2} + j^2 - \frac{j}{U^2 C}. \tag{A.44}$$

The number of grids in one scale is calculated by summing up P_{ij}^{rg} of all orientations:

$$N_i^{rg} = \sum_{j=1}^{\frac{1}{C}} 3P_{ij}^{rg} = \sum_{j=1}^{\frac{1}{C}} 3\left(\frac{1}{U^4 C^2} + j^2 - \frac{j}{U^2 C}\right), \tag{A.45}$$

where it is considered that geometric scaling of discretization requires different grids for different scales, thus three times more cell is required (Fig. A.2 and A.7). Performing the summation for the orientations and keeping the leading order only results in:

$$N_i^{rg} \approx 3\left(\frac{1}{U^4 C^3} + \frac{1}{3C^3} - \frac{1}{2U^2 C^3}\right). \tag{A.46}$$

The total number of required cells is expressed as the sum of N_i^{rg} for all scales:

$$N^{rg} = \sum_{i=1}^{\sigma^r(D_{max})} N_i^{rg} = \sum_{i=1}^{\sigma^r(D_{max})} 3\left(\frac{1}{U^4C^3} + \frac{1}{3C^3} - \frac{1}{2U^2C^3}\right). \tag{A.47}$$

The summation for the scales leads to:

$$N^{rg} \approx 3\frac{\sigma^r(D_{max})}{C^3}\left(\frac{1}{U^4} + \frac{1}{3} - \frac{1}{2U^2}\right). \tag{A.48}$$

Replacing $\sigma^r(D_{max})$ according to Eq. A.30 and $U = \frac{\sqrt{3}}{2}$ yields:

$$N^{rg} \approx \frac{13}{3}\frac{1}{C^3}\left(1 + \frac{\log(\frac{D_{max}}{S_1})}{\log\left(\frac{UC+2}{UC-2}\right)}\right) \approx 4.33\frac{1}{C^3}\left(1 + \frac{\log(\frac{D_{max}}{S_1})}{\log\left(\frac{UC+2}{UC-2}\right)}\right). \tag{A.49}$$

In each of the three overlapping population, in each scale and orientation only one grid cell is activated at the actual position of the rat, thus similarly to Eq. A.21, the number of simultaneously active grid cells is:

$$I^{rg} = \sum_{i=1}^{\sigma^r(D_{max})} \sum_{j=1}^{1/C} 3 = \frac{3}{2C}\sigma^r(D_{max}) = \frac{3}{2C}\left(\frac{\log\frac{D_{max}}{S_1}}{\log\frac{2+CU}{2-CU}} + 1\right). \tag{A.50}$$

Bibliography

Abe, K., Niikura, Y., and Misawa, M. (2003). The induction of long-term potentiation at amygdalo-hippocampal synapses in vivo. *Biological & Pharmaceutical Bulletin*, 26:1560–1562.

Acsády, L. and Káli, S. (2007). Models, structure, function: the transformation of cortical signals in the dentate gyrus. *Progress in Brain Research*, 163:577–599.

Ainge, J., Tamosiunaite, M., Woergoetter, F., and Dudchenko, P. (2007). ippocampal ca1 place cells encode intended destination on a maze with multiple choice points. *Journal of Neuroscience*, 27:9769–9779.

Andersen, P., Morris, R., Amaral, D., Bliss, T., and O'Keefe, J. (2007). *The Hippocampus Book (Oxford Neuroscience Series)*.

Baeg, E. H., Kim, Y. B., Huh, K., Mook-Jung, I., Kim, H. T., and Jung, M. W. (2003). Dynamics of population code for working memory in the prefrontal cortex. *Neuron*, 40(1):177–188.

Barry, C., Hayman, R., Burgess, N., and Jeffery, K. J. (2007). Experience-dependent rescaling of entorhinal grids. *Nature Neuroscience*, 10(6):682–684.

Bernander, O., Douglas, R. J., Martin, K. A., and Koch, C. (1991). Synaptic background activity influences spatiotemporal integration in single pyramidal cells. *Proc Natl Acad Sci USA*, 88(24):11569–11573.

Blair, H. T., Welday, A. C., and Zhang, K. (2007). Scale-invariant memory representations emerge from Moiré interference between grid fields that produce theta oscillations: a computational model. *Journal of Neuroscience*, 27:3211–3229.

Blaise, J. H. and Bronzino, J. D. (2003). Effects of stimulus frequency and age on bidirectional synaptic plasticity in the dentate gyrus of freely moving rats. *Experimental Neurology*, 182:1497–1506.

Bragin, A., Jandó, G., Nádasdy, Z., van Landeghem, M., and Buzsáki, G. (1995). Dentate eeg spikes and associated interneuronal population bursts in the hippocampal hilar region of the rat. *Journal of Neurophysiology*, 73:1691–1705.

Bramham, C. R. (1998). Phasic boosting of medial perforant path-evoked granule cell output time-locked to spontaneous dentate EEG spikes in awake rats. *Journal of Neurophysiology*, 79:2825–2832.

Brody, C. D., Hernandez, A., Zainos, A., and Romo, R. (2003). Timing and neural encoding of somatosensory parametric working memory in macaque prefrontal cortex. *Cereb Cortex*, 13(11):1196–1207.

Buhot, M. C., Foreman, N., Poucet, B., and Save, E. (1992). Object exploration and reactions to spatial and nonspatial changes in hooded rats following damage to parietal cortex or hippocampal formation. *Behavioral Neuroscience*, 106:447–456.

Burak, Y., Brookings, T., and Fiete, I. (2006). Triangular lattice neurons may implement an advanced numeral system to precisely encode rat position over large ranges.

Burgess, N., Barry, C., and O'Keefe, J. (2007). An oscillatory interference model of grid cell firing. *Hippocampus*, 17:801–812.

Buzsáki, G. (2002). Theta oscillations in the hippocampus. *Neuron*, 33(3):325–340.

Buzsáki, G. and Draguhn, A. (2004). Neuronal oscillations in cortical networks. *Science*, 304(5679):1926–1929.

Chavarriaga, R., Strösslin, T., Sheynikhovich, D., and Gerstner, W. (2005). A computational model of parallel navigation systems in rodents. *Neurocoinformatics*, 3:223–241.

Chen, L., Lin, L., Green, E., Barnes, C., and McNaughton, B. (1994). Head-direction cells in the rat posterior cortex. i. anatomical distribution and behavioral modulation. *Exp Brain Res*, 101:8–23.

Cook, E. P. and Johnston, D. (1997). Active dendrites reduce location dependent variability of synaptic input trains. *J Neurophysiol*, 78:2116–2128.

Csicsvári, J., Hirase, H., Czurkó, A., Mamiya, A., and Buzsáki, G. (1999). Oscillatory coupling of hippocampal pyramidal cells and interneurons in the behaving rat. *J Neurosci*, 19(1):274–287.

Deadwyler, S. A. and Hampson, R. E. (2004). Differential but complementary mnemonic functions of the hippocampus and subiculum. *Neuron*, 42(3):465–476.

Destexhe, A., Mainen, Z. F., and Sejnowski, T. J. (1998). Kinetic models of synaptic transmission. In Koch, C. and Segev, I., editors, *Methods in neuronal modeling*, A Bradford Book, pages 251–291. MIT Press, Cambridge, MA, 2 edition.

Destexhe, A. and Pare, D. (1999). Impact of network activity on the integrative properties of neocortical pyramidal neurons in vivo. *J Neurophysiol*, 81(4):1531–1547.

Destexhe, A., Rudolph, M., and Paré, D. (2003). The high-conductance state of neocortical neurons in vivo. *Nat Rev Neurosci*, 4(9):739–751.

Dolorfo, C. L. and Amaral, D. G. (1999). Entorhinal cortex of the rat: Topographic organization of the cells of origin of the perforant path projection to the dentate gyrus. *Journal of Comparative Neurology*, 398(1):25–48.

Ermentrout, B. (1996). Type I membranes, phase resetting curves, and synchrony. *Neural Comput*, 8(5):979–1001.

Fell, J., Klaver, P., Elfadil, H., Schaller, C., Elger, C. E., and Fernandez, G. (2003). Rhinal-hippocampal theta coherence during declarative memory formation: interaction with gamma synchronization? *Eur J Neurosci*, 17(5):1082–1088.

Foster, D. J., Morris, R. G. M., and Dayan, P. (2000). A model of hippocampally dependent navigation, using the temporal difference learning rule. *Hippocampus*, 10:1–16.

Frank, L. M., Brown, E. N., and Wilson, M. A. (2001). A comparison of the firing properties of putative excitatory and inhibitory neurons from CA1 and the entorhinal cortex. *J Neurophysiol*, 86(4):2029–2040.

Franzius, M., Vollgraf, R., and Wiskott, L. (2006). From grids to places. *Journal of Computatuional Neuroscience*, 22:297–299.

Freund, T. F. and Buzsáki, G. (1996). Interneurons of the hippocampus. *Hippocampus*, 6:347–470.

Fuhs, M. C. and Touretzky, D. S. (2006). A spin glass model of path integration in rat medial entorhinal cortex. *Journal of Neuroscience*, 26:4266–4276.

Fyhn, M., Hafting, T., Treves, A., Moser, M.-B., and Moser, E. I. (2007). Hippocampal remapping and grid realignment in entorhinal cortex. *Nature*, 446:190–194.

Fyhn, M., Molden, S., Witter, M. P., Moser, E. I., and Moser, M.-B. (2004). Spatial representation in the entorhinal cortex. *Science*, 305:1258–1264.

Gallistel, C. R. (1990). *The Organization of Learning.* Press/Bradford Books, MA.

Gevins, A., Smith, M. E., McEvoy, L., and Yu, D. (1997). High-resolution EEG mapping of cortical activation related to working memory: effects of task difficulty, type of processing, and practice. *Cereb Cortex*, 7(4):374–385.

Gilbert, P. E., Kesner, R. P., and DeCoteau, W. E. (1989). The role of the hippocampus in mediating spatial pattern separation. *Journal of Neuroscience*, 18:804–810.

Gilbert, P. E., Kesner, R. P., and Lee, I. (2001). Dissociating hippocampal subregions: A double dissociation between dentate gyrus and CA1. *Hippocampus*, 11(626–636).

Gillies, M. J., Traub, R. D., LeBeau, F. E., Davies, C. H., Gloveli, T., Buhl, E. H., and Whittington, M. A. (2002). A model of atropine-resistant theta oscillations in rat hippocampal area CA1. *J Physiol*, 543(Pt 3):779–793.

Givens, B. S. (1996). Stimulus-evoked resetting of the dentate theta rhythm: relation to working memory. *Neuroreport*, 8(1):159–163.

Givens, B. S. and Olton, D. S. (1990). Cholinergic and GABAergic modulation of medial septal area: effect on working memory. *Behav Neurosci*, 104(6):849–855.

Gold, J. I. and Shadlen, M. N. (2002). Banburismus and the brain: decoding the relationship between sensory stimuli, decisions, and rewards. *Neuron*, 36:299–308.

Golding, N. L. and Spruston, N. (1998). Dendritic sodium spikes are variable triggers of axonal action potentials in hippocampal ca1 pyramidal neurons. *Neuron*, 21(5):1189–1200.

Golding, N. L., Staff, N. P., and Spruston, N. (2002). Dendritic spikes as a mechanism for cooperative long-term potentiation. *Nature*, 418(6895):326–331.

Goldman, M. S., Levine, J. H., Major, G., Tank, D. W., and Seung, H. S. (2003). Robust persistent neural activity in a model integrator with multiple hysteretic dendrites per neuron. *Cereb Cortex*, 13(11):1185–1195.

Goodrich-Hunsaker, N. J., Hunsaker, M. R., and Kesner, R. P. (2008). The interactions and dissociations of the dorsal hippocampus subregions: how the dentate gyrus, CA3, and CA1 process spatial information. *Behavioral Neuroscience*, 122:16–26.

Guanella, A., Kiper, D., and Verschure, P. (2007). A model of grid cells based on a twisted torus topology. *International Journal of Neural Systems*, 17:231–240.

Hafting, T., Fyhn, M., Molden, S., Moser, M.-B., and Moser, E. I. (2005). Microstructure of a spatial map in the entorhinal cortex. *Nature*, 436:801–806.

Hausser, M., Spruston, N., and Stuart, G. J. (2000). Diversity and dynamics of dendritic signaling. *Science*, 290(5492):739–744.

Helmchen, F., Fee, M. S., Tank, D. W., and Denk, W. (2001). A miniature head-mounted two-photon microscope. High-resolution brain imaging in freely moving animals. *Neuron*, 31(6):903–912.

Huxter, J., Burgess, N., and O'Keefe, J. (2003). Independent rate and temporal coding in hippocampal pyramidal cells. *Nature*, 425(6960):828–832.

Jeffery, K. J. and Burgess, N. (2006). A metric for the cognitive map: Found at last? *Trends In Cognitive Science*, 10(1):1–3.

Jensen, O. and Lisman, J. (2005). Hippocampal sequence-encoding driven by a cortical multi-item working memory buffer. *Trends Neurosci*, 28(2):67–72.

Jensen, O. and Lisman, J. E. (1996). Hippocampal CA3 region predicts memory sequences: accounting for the phase precession of place cells. *Learn Mem*, 3:279–287.

Jensen, O. and Lisman, J. E. (1998). An oscillatory short-term memory buffer model can account for data on the Sternberg task. *J Neurosci*, 18(24):10688–10699.

Jensen, O. and Tesche, C. D. (2002). Frontal theta activity in humans increases with memory load in a working memory task. *Eur J Neurosci*, 15(8):1395–1399.

Jung, M. W. and McNaughton, B. L. (1993). Spatial selectivity of unit activity in the hippocampal granular layer. *Hippocampus*, 3:165–182.

Jung, M. W., Wiener, S. I., and McNaughton, B. L. (1994). Comparison of spatial firing characteristics of units in dorsal and ventral hippocampus of the rat. *Journal of Neuroscience*, 14:7347–7356.

Kahana, M. J., Seelig, D., and Madsen, J. R. (2001). Theta returns. *Curr Opin Neurobiol*, 11(6):739–744.

Káli, S. and Dayan, P. (2000). The involvement of recurrent connections in area CA3 in establishing the properties of place fields: a model. *Journal of Neuroscience*, 20:7463–7477.

Kamondi, A., Acsády, L., Wang, X.-J., and Buzsáki, G. (1998). Theta oscillation in somata and dendrites of hippocampal pyramidal cells in vivo: activity-dependent phase-precession of action potentials. *Hippocampus*, 8:244–261.

Kandel, E. R. and Spencer, W. A. (1961). Electrophysiology of hippocampal neurons. IV. fast prepotentials. *J Neurophysiol*, 24(272–285).

Klausberger, T., Magill, P. J., Márton, L. F., Roberts, J. D., Cobden, P. M., Buzsáki, G., and Somogyi, P. (2003). Brain-state- and cell-type-specific firing of hippocampal interneurons *in vivo*. *Nature*, 421(6925):844–848.

Koulakov, A. A., Raghavachari, S., Kepecs, A., and Lisman, J. E. (2002). Model for a robust neural integrator. *Nat Neurosci*, 5(8):775–782.

Kubie, J. L., Muller, R. U., and Bostock, E. (1990). Spatial firing properties of hippocampal theta-cells. *Journal of Neuroscience*, 10(4):1110–1123.

Lee, H., Simpson, G. V., Logothetis, N. K., and Rainer, G. (2005). Phase locking of single neuron activity to theta oscillations during working memory in monkey extrastriate visual cortex. *Neuron*, 45(1):147–156.

Lengyel, M. and Érdi, P. (2004). Theta modulated feed-forward network generates rate and phase coded firing in the entorhino-hippocampal system. *IEEE Trans Neural Netw*, 15:1092–1099.

Lengyel, M., Szatmáry, Z., and Érdi, P. (2003). Dynamically detuned oscillations account for the coupled rate and temporal code of place cell firing. *Hippocampus*, 13(6):700–714.

Leung, L. S. and Yim, C. Y. (1986). Intracellular records of theta rhythm in hippocampal CA1 cells of the rat. *Brain Res*, 367(1-2):323–327.

Leutgeb, J. K., Leutgeb, S., Moser, M.-B., and Moser, E. I. (2007). Pattern separation in the dentate gyrus and CA3 of the hippocampus. *Science*, 315:961–966.

Levitt, T. S. and Lawton, D. T. (1990). Qualitative navigation for mobile robots. *Artificial Intelligence*, 44:305–360.

Lisman, J. E. and Idiart, M. A. P. (1995). Storage of 7 ± 2 short-term memories in oscillatory subcycles. *Science*, 267:1512–1515.

Loewenstein, Y., Mahon, S., Chadderton, P., Kitamura, K., Sompolinsky, H., Yarom, Y., and Hausser, M. (2005). Bistability of cerebellar purkinje cells modulated by sensory stimulation. *Nat Neurosci*, 8(2):202–211.

Machens, C. K., Romo, R., and Brody, C. D. (2005). Flexible control of mutual inhibition: a neural model of two-interval discrimination. *Science*, 307:1121–1124.

Macrides, F., Eichenbaum, H. B., and Forbes, W. B. (1982). Temporal relationship between sniffing and the limbic theta rhythm during odor discrimination reversal learning. *J Neurosci*, 2(12):1705–1717.

Magee, J., Hoffman, D., Colbert, C., and Johnston, D. (1998). Electrical and calcium signaling in dendrites of hippocampal pyramidal neurons. *Annu Rev Physiol*, 60:327–346.

Magee, J. C. (1999). Dendritic I_h normalizes temporal summation in hippocampal CA1 neurons. *Nat Neurosci*, 2(6):508–514.

Major, G. and Tank, D. (2004). Persistent neural activity: prevalence and mechanisms. *Curr Opin Neurobiol*, 14(6):675–684.

Marder, E., Abbott, L. F., Turrigiano, G. G., Liu, Z., and Golowasch, J. (1996). Memory from the dynamics of intrinsic membrane currents. *Proc Natl Acad Sci USA*, 93(24):13481–13486.

Marshall, L., Henze, D. A., Hirase, H., abd G Dragoi, X. L., and Buzsaki, G. (2002). Hippocampal pyramidal cell-interneuron spike transmission is frequency dependent and responsible for place modulation of interneuron discharge. *Journal of Neuroscience*, 22(2).

McNaughton, B. L., Barnes, C. A., Gerrard, J. L., Gothard, K., Jung, M. W., Knierim, J. J., Kudrimoti, H., Qin, Y., Skaggs, W. E., Suster, M., and Weaver, K. L. (1996). Deciphering the hippocampal polyglott: the hippocampus as a path integration system. *J Exp Biol*, 199:173–185.

McNaughton, B. L., Barnes, C. A., and O'Keefe, J. (1983). The contributions of position, direction, and velocity to single unit activity in the hippocampus of freely-moving rats. *Exp Brain Res*, 52:41–49.

Mehta, M. R., Lee, A. K., and Wilson, M. A. (2002). Role of experience and oscillations in transforming a rate code into a temporal code. *Nature*, 417(6890):741–746.

Menzel, E. W. (1973). Chimpanzee spatial memory organization. *Science*, 182:943–945.

Mizuhara, H., Wang, L. Q., Kobayashi, K., and Yamaguchi, Y. (2004). A long-range cortical network emerging with theta oscillation in a mental task. *Neuroreport*, 15(8):1233–1238.

Mizumori, S. J., Perez, G. M., Alvado, M. C., Barnes, C. A., and McNaughton, B. L. (1990). Reversible inactivation of the medial septum differentially affects two forms of learning in rats. *Brain Res*, 528(1):12–20.

Moser, E. I., Kropff, E., and Moser, M.-B. (2008). Place cells, grid cells, and the brain's spatial representation system. *Annual Review of Neuroscience*, 31.

Nakao, K., Matsuyama, K., Matsuki, N., and Ikegaya, Y. (2004). Amygdala stimulation modulates hippocampal synaptic plasticity. *Proceedings of the National Academy of Sciences*, 101:14270–14275.

O'Keefe, J. and Dostrovsky, J. (1971). The hippocampus as a spatial map. Preliminary evidence from unit activity in the freely moving rat. *Brain Res*, 34:171–175.

O'Keefe, J. and Recce, M. L. (1993). Phase relationship between hippocampal place units and the EEG theta rhythm. *Hippocampus*, 3:317–330.

Pan, W. X. and McNaughton, N. (1997). The medial supramammillary nucleus, spatial learning and the frequency of hippocampal theta activity. *Brain Res*, 764(1–2):101–108.

Pare, D. (1995). Amygdalo-entorhinal relations and their reflection in the hippocampal formation: generation of sharp sleep potentials. *Journal of Neuroscience*, 15:2482–2503.

Penttonen, M., Kamondi, A., Sik, A., Acsády, L., and Buzsáki, G. (1997). Feed-forward and feed-back activation of the dentate gyrus in vivo during dentate spikes and sharp wave bursts. *Hippocampus*, 7:437–450.

Pinsky, P. F. and Rinzel, J. (1994). Intrinsic and network rythmogenesis in a reduced Traub model for CA3 neurons. *J Comput Neurosci*, 1:39–60.

Poirazi, P., Brannon, T., and Mel, B. W. (2003). Pyramidal neuron as two-layer neural network. *Neuron*, 37(6):989–999.

Poucet, B., Thinus-Blanc, C., and Chapuis, N. (1983). Route-planning in cats, in relation to the visibility of the goal. *Animal Behaviour*, 31(2):594–599.

Rall, W. (1959). Branching dendritic trees and motoneuron membrane resistivity. *Exp Neurol*, 1:491–527.

Rall, W. (1989). Cable theory for dendritic neurons. In Koch, C. and Segev, I., editors, *Methods in neuronal modeling*, pages 29–38, Cambridge, MA. The MIT Press.

Ranck, J. (1984). Head-direction cells in the deep layers of the dorsal presubiculum in freely moving rats. *Soc Neurosci Abstr*, 10:599.

Redish, A. D. and Touretzky, D. S. (1997). Cognitive maps beyond the hippocampus. *Hippocampus*, 7(1):15–35.

Redish, D. A., McNaughton, B. L., and Barnes, C. A. (2000). Place cell firing shows an inertia-like process. *Neurocomputing*, 32–33:235–241.

Reyes, A. (2001). Influence of dendritic conductances on the input-output properties of neurons. *Annu Rev Neurosci*, 24:653–675.

Rolls, E. T. and Kesner, R. P. (2006). A computational theory of hippocampal function, and empirical tests of the theory. *Progress in Neurobiology*, 79:1–48.

Rudolph, M. and Destexhe, A. (2003a). A fast-conducting, stochastic integrative mode for neocortical neurons in vivo. *J Neurosci*, 23(6):2466–2476.

Rudolph, M. and Destexhe, A. (2003b). Tuning neocortical pyramidal neurons between integrators and coincidence detectors. *J Comput Neurosci*, 14(3):239–251.

Samsonovich, A. and McNaughton, B. L. (1997). Path integration and cognitive mapping in a continuous attractor neural network model. *J Neurosci*, 17(15):5900–5920.

Sargolini, F., Fyhn, M., Hafting, T., McNaughton, B. L., Witter, M. P., Moser, M.-B., and Moser, E. I. (2006). Conjunctive representation of position, direction, and velocity in entorhinal cortex. *Science*, 312:758–762.

Sarnthein, J., Petsche, H., Rappelsberger, P., Shaw, G. L., and von Stein, A. (1998). Synchronization between prefrontal and posterior association cortex during human working memory. *Proc Natl Acad Sci USA*, 95(12):7092–7096.

Sauseng, P., Klimesch, W., Doppelmayr, M., Hanslmayr, S., Schabus, M., and Gruber, W. R. (2004). Theta coupling in the human electroencephalogram during a working memory task. *Neurosci Lett*, 354(2):123–126.

Schwindt, P. and Crill, W. (1999). Mechanisms underlying burst and regular spiking evoked by dendritic depolarization in layer 5 cortical pyramidal neurons. *J Neurophysiol*, 81(3):1341–1354.

Seidenbecher, T., Laxmi, T. R., Stork, O., and Pape, H. C. (2003). Amygdalar and hippocampal theta rhythm synchronization during fear memory retrieval. *Science*, 301(5634):846–850.

Seung, H. S. (1996). How the brain keeps the eyes still. *Proc Natl Acad Sci USA*, 93(23):13339–13344.

Sharp, P. E. (1997). Subicular cells generate similar spatial firing patterns in two geometrically and visually distinctive environments: comparison with hippocampal place cells. *Behav Brain Res*, 85(1):71–92.

Siegrist, C., Etienne, A. S., Boulens, V., Maurer, R., and Rowe, T. (2003). Homing by path integration in a new environment. *Animal Behaviour*, 65:185–194.

Skaggs, W. E., McNaughton, B. L., Wilson, M. A., and Barnes, C. A. (1996). Theta phase precession in hippocampal neuronal populations and the compression of temporal sequences. *Hippocampus*, 6:149–172.

Solstad, T., Moser, E. I., and Einevoll, G. T. (2006). From grid cells to place cells: a mathematical model. *Hippocampus*, 16:1026–1031.

Soltész, I. and Deschenes, M. (1993). Low- and high-frequency membrane potential oscillations during theta activity in CA1 and CA3 pyramidal neurons of the rat hippocampus under ketamine-xylazine anesthesia. *J Neurophysiol*, 70:97–116.

Stackman, R. and Taube, J. (1998). Firing properties of rat lateral mammillary single units: head direction, head pitch, and angular head velocity. *J Neurosci*, 18:9020—9037.

Stam, C. J., van Cappellen van Walsum, S., and Micheloyannis, S. (2002). Variability of EEG synchronization during a working memory task in healthy subjects. *Int J Psychophysiol*, 46(1):53–66.

Taube, J. (1995). Head direction cells recorded in the anterior thalamic nuclei of freely moving rats. *J Neurosci*, 15:70–86.

Tesche, C. D. and Karhu, J. (2000). Theta oscillations index human hippocampal activation during a working memory task. *Proc Natl Acad Sci USA*, 97(2):919–924.

Trullier, O. and Meyer, J.-A. (2000). Animat navigation using a cognitive graph. *Biological Cybernetics*, 83:271–285.

Trullier, O., Wiener, S. I., Berthoz, A., and Meyer, J.-A. (1997). Biologically based artificial navitagtion systems: review and prospects. *Progress in Neurobiology*, 51:483–544.

Tsodyks, M. V., Skaggs, W. E., Sejnowski, T. J., and McNaughton, B. L. (1996). Population dynamics and theta phase precession of hippocampal place cell firing: a spiking neuron model. *Hippocampus*, 6:271–280.

Ujfalussy, B., Erős, P., Somogyvári, Z., and Kiss, T. (2008). Episodes in space: A modelling study of hippocampal place representation. In *Lecture Notes in Artificial Intelligence 5040*, Proceedings of the SAB 2008, pages 123–136. Springer-Verlag Berlin Heidelberg.

Vetter, P., Roth, A., and Hausser, M. (2001). Propagation of action potentials in dendrites depends on dendritic morphology. *J Neurophysiol*, 85(2):926–937.

Wallenstein, G. V. and Hasselmo, M. E. (1997). GABAergic modulation of hippocampal activity: sequence learning, place field development, and the phase precession effect. *J Neurophysiol*, 78:393–408.

Wei, D. S., Mei, Y. A., Bagal, A., Kao, J. P., Thompson, S. M., and Tang, C. M. (2001). Compartmentalized and binary behavior of terminal dendrites in hippocampal pyramidal neurons. *Science*, 293(5538):2272–2275.

Wiener, S. (1993). Spatial and behavioral correlates of striatal neurons in rats performing a self-initiated navigation task. *J Neurosci*, 13:3802–3817.

Williams, S. R. (2004). Spatial compartmentalization and functional impact of conductance in pyramidal neurons. *Nat Neurosci*, 7(9):961–967.

Williams, S. R. and Stuart, G. J. (2003). Role of dendritic synapse location in the control of action potential output. *Trends Neurosci*, 26(3):146–154.

Winson, J. (1978). Loss of hippocampal theta rhythm results in spatial memory deficit in the rat. *Science*, 201(4351):160–163.

Wong, R. K., Prince, D. A., and Basbaum, A. I. (1979). Intradendritic recordings from hippocampal neurons. *Proc Natl Acad Sci USA*, 76(2):986–990.

Yamaguchi, Y. (2003). A theory of hippocampal memory based on theta phase precession. *Biol Cybern*, 89(1):1–9.

Yamaguchi, Y., Aota, Y., McNaughton, B. L., and Lipa, P. (2002). Bimodality of theta phase precession in hippocampal place cells in freely running rats. *J Neurophysiol*, 87:2639–2642.

Ylinen, A., Soltész, I., Bragin, A., Penttonen, M., Sík, A., and Buzsáki, G. (1995). Intracellular correlates of hippocampal theta rhythm in identified pyramidal cells, granule cells, and basket cells. *Hippocampus*, 5(1):78–90.

Zugaro, M. B., Monconduit, L., and Buzsáki, G. (2005). Spike phase precession persists after transient intrahippocampal perturbation. *Nat Neurosci*, 8(1):67–71.

Summary

The present dissertation focuses on the functioning of neurons and neural networks that form the basis for the navigation ability of rodents. In the first part we study hippocampal *place cells* that encode the location of the animal. Place cells provide prototypical examples of neurons firing jointly phase and rate-coded spike trains. We propose a biophysical mechanism accounting for the generation of place cell firing at the single neuron level. An interplay between external theta-modulated excitation impinging the dendrite and intrinsic dendritic spiking as well as between frequency-modulated dendritic spiking and somatic membrane potential oscillations was a key element of the model. Through these interactions robust phase and rate-coded firing emerged in the model place cell, reproducing salient experimentally observed properties of place cell firing. The model showed long-term integration in single cells which can lead to persistent neural activity lasting for seconds after transient stimulation. We discuss the plausibility of our proposed mechanism and its potential to account for the firing pattern of cells outside the hippocampus during working memory tasks.

In the second part we study the role of entorhinal cortical *grid cells* in spatial navigation. This ability requires the animal to keep track its direction and distance from specific locations. In rodents, direction of the animal is encoded by the activity of head direction cells, but distance information is only indirectly available. A neural system downstream from the entorhinal cortex seems to be necessary to extract the distance information from the periodic activity of grid cells. We propose that a system of such *distance cells* store the distance of the animal from important locations in the dentate gyrus region of the hippocampus. First, we show analytically that the grid cell system forms an optimal representation of places for the purpose of distance estimation in terms of the number of necessary neurons and the extent of the average firing activity of the neural network. Second, a computational model is set up to study the neural mechanism of distance information decoding from the ensemble of grids cells. Simulation results of this model verifies that the activity of the distance cell population is able to unambiguously encode the distance of the animal from important places. The proposed distance cells have a multi-peaked spatial activity pattern similar to the firing pattern of granule cells in dentate gyrus.

Összefoglalás

Jelen disszertáció a rágcsálók térbeli tájékozódási és navigációs képességeit megalapozó idegsejtekkel és idegsejt hálózatokkal foglalkozik. A disszertáció első részében a hippokampuszban található helysejteket tanulmányozom, amelyek az állat térbeli elhelyezkedését kódolják. A helysejtek tüzelési fázisa és frekvenciája is az állat térbeli pozíciójának függvénye. Egy olyan mechanizmust javaslok a helysejtek tüzelési mintázatának kialakulására, amely egysejt szinten magyarázza ezen fázis- és ráta kód létrejöttét. A javasolt modellben a dendritre érkező periodikus serkentés (theta-oszcilláció) és az intrinszik generált dendritikus akciós potenciálok, valamint a frekvencia-modulált dendritikus tüzelések és a szomatikus membránpotenciál oszcilláció közötti kölcsönhatások voltak a kulcselemek. Ezen sejtszintű interakciók hatására a modell neuron a kísérleti megfigyelésekkel részleteiben is összhangban lévő tüzelési mintázatot mutat. A modell sejt képes a bemenetek hosszú-távú integrációjára, ami a neuronok perzisztens, stimulációt követően másodpercekig fennálló aktivitásához vezethet. A javasolt mechanizmus szerepet játszhat a munkamemória kialakításában részt vevő, hippokampuszon kívüli idegsejtek működésében is.

A második részben az entorhinális kéregben található grid sejtek térbeli tájékozódásban betöltött szerepét tanulmányozom. A navigációhoz szükséges, hogy az állat „észben tartsa" a különböző helyeknek az aktuális pozíciótól való irányát és távolságát. Rágcsálókban az állat mozgási irányát a fej-irány sejtek kódolják, távolságot kódoló idegsejteket viszont mindeddig nem találtak az idegrendszerben. Hipotézisünk szerint ezek a távolságsejtek vélhetően az entorhinális kéreg kimeneti régiójában, a gyrus dentatusban találhatóak, és a grid sejtek aktivitásából olvassák ki a távolság információt. Analitikus számításokkal megmutatjuk, hogy a grid sejt rendszer optimális helyreprezentációt biztosít a távolság kódolás számára, mind a szükséges idegsejtek számának, mind pedig a rendszer átlagos tüzelési aktivitásának tekintetében. Egy sejthálózati modellt javaslunk, amin a távolság információ kiolvasási mechanizmusát tanulmányozzuk. A modell szimulációk alátámasztják, hogy a távolságsejtek aktivitása alkalmas arra, hogy egyértelműen kódolja az állat más helyektől való távolságát. A szimulált távolságsejtek térbeli tüzelési mintázata hasonlít a gyrus dentatusban található szemcsejtek aktivitásmintázatára.